Study of ceria-composite materials for high-temperature CO2 capture and their ruthenium functionalization for methane production

Catalysis Today 429 (2024) 114478

Contents lists available at ScienceDirect

Catalysis Today

journal homepage: www.elsevier.com/locate/cattod

Study of ceria-composite materials for high-temperature CO_2 capture and their ruthenium functionalization for methane production☆

Andrea Rizzetto, Marco Piumetti *, Raffaele Pirone, Enrico Sartoretti, Samir Bensaid

Department of Applied Science and Technology (DISAT), Politecnico di Torino, Corso Duca degli Abruzzi 24, 10129 Turin, Italy

ARTICLE INFO

Keywords:
Dual function materials
CO_2 adsorption
Methanation
Ruthenium
Ceria
ZSM-5
Alumina

ABSTRACT

A set of Dual Function Materials (DFMs) was prepared to seize the CO_2 from a rich feed gas and to in-situ convert it to methane (synthetic natural gas). Specifically, ruthenium-ceria composite materials were synthesized through successive impregnation depositions on two high surface area supports, namely Al_2O_3 and ZSM-5. Cerium oxide has both the roles of CO_2 adsorbent and promoter support for ruthenium, which represents the active component for methanation. Three different quantities of ceria (10, 20, and 30 wt%) were dispersed onto the solid supports, and the adsorption capacities of the ceria-based materials were studied at different temperatures (150, 200, and 250 °C) at atmospheric pressure. The samples exhibiting the best results in terms of CO_2 adsorption (30 wt% CeO_2/Al_2O_3 and 30 wt% CeO_2/ZSM-5) were subsequently impregnated to obtain ruthenium-loaded catalysts (2 wt% Ru). These functionalized materials were characterized by XRD, N_2 physisorption at −196 °C, TPDRO, ICP-MS, XPS, FESEM, HRTEM, and FT-IR. Then, cyclic experiments of CO_2 adsorption and methanation were performed, simulating a real use of the catalysts at 250 °C and atmospheric pressure. The deposition of ruthenium-ceria on a high surface area support was found to be crucial for maintaining the methanation activity of this catalytic system under cyclic CO_2 adsorption-hydrogenation conditions. The Al_2O_3-supported ruthenium-ceria catalyst adsorbed a lower amount of CO_2 (ca. 200 μmol g^{-1} per each cycle) with respect to the zeolite-supported sample (ca. 300 μmol g^{-1}); nevertheless, the former material presented the best methanation performances, thanks to an intermediate ruthenium-ceria interaction, yielding a maximum of 51% of CO_2 converted and producing up to 111 μmol g^{-1} of CH_4.

1. Introduction

The growth of the world population, urbanization, modernization, and industrialization has produced the increment in global energy demand in recent years. Fossil fuels such as crude oil, coal, and natural gas are the most essential energy carries, providing almost 85% of the world's primary energy. Due to a massive exploitation of fossil fuels, a huge quantity of anthropogenic greenhouse gases (GHGs) is released into the atmosphere, mostly in the form of carbon dioxide (CO_2). This policy has resulted in global warming, climate change, and various other associated environmental trouble, as well as acid rains, extreme weather events, imbalanced food distribution, and mass migration of birds and other animals [1–3].

These environmental mutations are expected to become irreversible, unless a concrete action is undertaken to reach a carbon-neutral society by 2050; hence, reducing greenhouse gas emissions is an urgent challenge that humankind is facing [4]. In parallel with the traditional carbon dioxide capture and storage systems (CCS), CO_2 capture, and utilization systems (CCUs) have recently developed since they allow to valorise CO_2, by converting the captured gas into products with market value. These capture and conversion approaches allow for the reduction of emissions and, at the same time, the generation of chemicals from non-fossil energy carries. The captured CO_2 is used as a reagent to mainly obtain two categories of products, i.e., synthetic fuels or chemical intermediates, which can be employed as building blocks in the chemical industry. From the point of view of the carbon balance, CCU systems do not involve a permanent sequestration of carbon dioxide (as occurs in the case of storage in deposits), but allow the conservation of resources, since the use of the conversion products will avoid the emission of new CO_2, coming from traditional fossil sources [5,6]. In recent years, research has investigated different systems for the hydrogenative conversion of CO_2 to produce valuable products, such as

☆ Supporting information for this article is given via a link at the end of the document.

* Corresponding author.
E-mail address: marco.piumetti@polito.it (M. Piumetti).

https://doi.org/10.1016/j.cattod.2023.114478
Received 12 July 2023; Received in revised form 10 November 2023; Accepted 29 November 2023
Available online 2 December 2023

methane (CH_4) [3], carbon monoxide (CO) [7], light olefines (C_nH_{2n}) [8], hydrocarbons (HC) [9,10], formic acid (HCOOH) [11], formaldehyde (HCHO) [12], dimethyl ether (DME) [13,14], methanol (CH_3OH) [15], and higher alcohols ($C_{2+}OH$) [16]. Among the different conversion alternatives, the methanation of CO_2 is the most favoured reaction according to thermodynamics [3]. In this case, the sequestered carbon dioxide is made to react with a stream of H_2 to produce synthetic natural gas (SNG) following Sabatier's reaction, Eq. (1):

$$CO_2 + 4H_2 \rightarrow CH_4 + 2H_2O \quad \Delta H = -165.0\text{kJ/mol} \tag{1}$$

where the enthalpy change (ΔH) value is referred to T = 25 °C and P = 0.1 MPa.

Many catalysts with different formulations have been prepared, characterized and tested for this reaction, such as transition metals (Fe, Ru, Co, Rh, Ir, Ni, Pd, Pt) dispersed on several oxide supports, including SiO_2, TiO_2, Al_2O_3, ZrO_2, CeO_2, or mixed oxides [17–19]. It has been observed that composite systems are able to enhance the conversion capabilities of catalysts, and several studies emphasized the synergistic effects between surface area, electronic/redox properties, structural characteristics, acidity/basicity, metal-support interactions, oxygen vacancies, and reducibility during catalytic activity [14,20–22]. Dual Function Materials (DFMs) have been developed to convert CO_2 to methane through a gas storage and direct conversion without the requirement for energy intensive CO_2 purification thermal processes. Typically, a DFM is composed by three components: a CO_2 sorption phase, a catalytically active metal (e.g., Ni, Ru, Rh)[23–25], and a high surface area support (such as Al_2O_3 or ZrO_2). After the first publication of a study about the use of DFMs by Duyar et al., several methanation catalysts containing alkaline and alkaline-earth metals were investigated [21,26]. The features of all phases are chosen so that the capture and the catalytic conversion can occur at the same temperature and pressure, thanks to the combination of the metal site, the adsorbent material, and the support features.

There is scientific evidence that the presence of metal oxides phases in composite catalysts improve catalytic performance thanks to the oxygen storage capacities (OSC), which can enhance active metal dispersion and participate in surface carbon conversion. Among the other oxides, CeO_2 has presently become a ubiquitous component in many catalytic systems thanks to its well-studied capability to work as oxygen buffer, storing/realising oxygen via the Ce^{3+}/Ce^{4+} redox couple. Moreover, ceria is able to remove the carbon deposited on the catalyst surface, thereby providing a solution to one of the major issues of catalytic systems [27–29]. The elevated amounts of oxygen vacancies also have beneficial effect on CO_2 adsorption/activation, making ceria-based catalysts highly active and selective to methane formation [30–37]. Along with ceria features, methanation is also favoured by the presence of reduced noble metal sites that, as well as having a role in the hydrogenation step, participate to CO_2 activation, irrespectively of the metal type [37–39]. Nickel is one of the most investigated metal phases used for the preparation of methanation catalysts: it is cost-effective, it has a great selectivity towards CH_4, and it can operate between 300 and 450 °C. However, Ni catalysts suffer from sintering and reverse water gas-shift reaction (RWGS) at high operating temperatures, which compromises CH_4 selectivity and CO_2 conversion [40]. Recently, research has moved towards the study of noble-metal-based catalysts such as Rh, Pt, Pd, and Ru [41–43] which exhibit a lower CO_2 methanation onset than Ni (from ca. 180 °C to ca. 250 °C) enabling to carry out catalytic processes at temperatures where the RWGS is thermodynamically unfavourable. Particularly, ruthenium has received great attention because it possesses optimum chemisorption energy, and a greater capacity to activate CO/CO_2 during methanation reactions with respect to the other metals of groups 8–10 [3].

In this work, the CO_2 adsorption capacity of ceria-based materials was investigated, exploring the possibility of developing a novel CO_2 sorbent material effective at temperatures that would be challenging for pristine CeO_2, zeolite and alumina. To increase CeO_2 surface area, the cerium precursor was impregnated on high surface area supports, Al_2O_3 and H-ZSM-5 zeolite. Before this work, other authors studied ceria-supported materials, for instance $Rh/CeO_2/SiO_2$ as catalyst for cellulose gasification [44] and CeO_2-doped Ni/Al_2O_3 [45] for the CO methanation. Tada et al. focused their research on CO_2 continuous methanation and developed a Ru/CeO_2-Al_2O_3 composite catalyst [46], observing the useful effect of the support on cerium oxide. Indeed, the oxide dispersion is expected to improve CO_2 adsorption per unit of catalyst weight and increase the number of utilizable oxygen vacancies for higher capture temperatures [46,47]. Ru-containing CeO_2 catalysts are usually recognized among the most active materials in the hydrogenation of CO_2 to methane thanks to their fundamental physico-chemical properties (vide supra). However, these systems need a continuous flow of CO_2 and H_2 to the catalytic phase. Thus, conversely to traditional Ru/CeO_2 catalysis, this work explored the possibility to develop new composite Dual Function Materials for a stepwise conversion of CO_2 to methane. For this purpose, cyclic methanation experiments were performed in order to investigate the capabilities of these catalysts, pushing the materials to operate under continuous sequences of adsorption and regeneration at constant temperature and pressure.

2. Materials and experimental methods

2.1. Chemicals

Six ceria-based materials with different amounts of CeO_2 (10, 20, and 30 wt%) were dispersed onto aluminium oxide and H-ZSM-5 with Si/Al ratio of 11.5 through an impregnation method (using 1 g of support). Cerium (III) nitrate hexahydrate ($Ce(NO_3)_3 \bullet 6H_2O$ – Sigma Aldrich, 99% trace metals basis) was used as cerium precursor for the preparation of the materials employed in the adsorption tests. Ammonium ZSM-5 Zeolite (Sigma Aldrich) and aluminium oxide, gamma-phase, 99.97% metals basis (Alfa Aesar) were the two supports impregnated. For the synthesis of the catalysts, ruthenium (III) nitrosyl nitrate solution in diluted nitric acid ($Ru(NO)(NO_3)_x(OH)_y, x+y=3-1,5\%Ru$ – Sigma Aldrich) was selected as ruthenium precursor. Cerium (IV) oxide (nanopowder, < 25 nm particle size – Sigma Aldrich) was used as standard materials for the CO_2-TPD and H_2-TPR analysis.

2.2. Materials preparation

The first part of this study was focused on the valuation of several materials based on supported cerium oxide for CO_2 adsorption at high temperature. All the materials in this work were synthetized through an impregnation method, adapted from the literature [46,48]. CeO_2/ZSM-5 catalysts were prepared by impregnating a 100 mL aqueous solution of cerium nitrate on 1 g of ZSM-5 powder. This zeolite was previously calcined at 550 °C in an air atmosphere for 5 h to obtain the protonated form, in order to make the support more stable to subsequent heat treatments. The zeolite was suspended in the cerium nitrate solution and the slurry was heated at 100 °C under stirring until complete water evaporation. Therefore, the samples were dried at 60 °C overnight and then calcined at 500 °C for 3 h in air with a heating rate of 2 °C/min. CeO_2/γ-Al_2O_3 catalysts were synthesized through the same procedure. The stoichiometric ratio of the reagents was calculated to obtain a nominal CeO_2 concentration of 10, 20, and 30 wt% for both the supports. Two Ru-base Dual Function Materials were prepared by employing a water solution of ruthenium (III) nitrosyl nitrate to impregnate dropwise 30%CeO_2/ZSM-5% and 30%CeO_2/Al_2O_3 samples. These materials were dried at 60 °C and then calcined at 500 °C for 3 h in air. The nominal Ru loading was 2 wt% for both samples. The following nomenclatures was assigned to the sorbent materials prepared in this work: xCA and xCZ, where "x" refers to the nominal ceria percentage loaded on the two supports (A – alumina; Z – zeolite). The Ru-containing catalysts,

2%Ru/30%CeO_2/Al_2O_3 and 2%Ru/30%CeO_2/ZSM-5, were hereafter abbreviated as 2R30CA and 2R30CZ, respectively.

2.3. Sample characterization

Cerium content of the samples was confirmed by using a Thermo Scientific iCAP RQ ICP-MS device. Powder catalysts were dissolved in a mixture of hydrofluoric acid, phosphoric acid, and sulfuric acid (2 mL: 4 mL: 4 mL) by the mean of microwave-assisted digestion at 220 °C for 15 min (heating rate 10 °C/min). Afterwards, the digestates were diluted to obtain the suitable metal concentration for the analysis.

X-Ray Diffraction (XRD) measurements were performed by the means of X Pert PANalytical diffractometer (Cu Kα radiation) equipped with a PiX accelerator detector. Powder data were collected on a flat zero background sample holder. Diffraction intensities were recorded from 10 to 80 2θ (voltage 40 kV; current 40 mA). Data analysis was carried out using the HighScore Plus® software to identify the phases characterizing the samples. The mean crystallite size of the phases was calculated thought Scherrer's equation (Eq. 2), where K is the shape factor (0.89), λ is X-ray wavelength (0.154 nm), β is the line broadening at half the maximum intensity in radians, and θ is Bragg angle. A LaB_6 standard was used to correct the instrumental peak broadening.

$$D(nm) = \frac{K\lambda}{\beta\cos\theta} \quad (2)$$

The specific surface areas of the materials were measured through nitrogen physisorption at 77 K, using a Micromeritics ASAP TRISTAR 3020 instrument. Before being analysed, all the samples underwent a pretreatment consisting in heating in nitrogen flow at 200 °C for 2 h. This step is performed in a specifically dedicated system (Micromeritics FlowPrep 060), to eliminate possible adsorbed components on the material. Calculation of specific surface area (SSA) was done using Brunauer-Emmett-Teller (BET) method with the acquisition of 10 points (relative pressure range from 0.05 to 0.3), while the pore volume and pore average size were evaluated by applying the Barrett-Joyner-Halenda (BJH) algorithm to the desorption branch. The micropore volume was calculated according to the t-plot method.

X-ray photoelectron spectroscopy (XPS) spectra were collected by the mean of a XPS PHI 5000 Versa Probe instrument (187.85 eV band-pass energy, 45° take-off angle, 100.0 μm X-ray spot size). Spectra were charge corrected so that the main line for the carbon 1 s spectrum (adventitious carbon) was set to 284.8 eV. The XPS bands were deconvolved through CasaXPS® processing software, version 2.3.25. The Ce^{3+}/Ce^{4+} surface atomic ratio was calculated according to the relative peak areas in Ce 3d XPS spectra [49]: in particular, four peaks were associated to Ce^{3+} (v°, v', u°, u') while other six peaks were ascribed to Ce^{4+} (v, v'', v''', u, u'', u''').

Morphological analysis was performed in a Zeiss Merlin with a Gemini-II column and an Oxford x-act X-ray detector. The powder was coated with a 5 nm thick layer of platinum via sputter deposition, before the analysis. FESEM-EDX mapping images of ruthenium-functionalized catalysts were collected in order to investigate the dispersion of CeO_2 and Ru species onto ZSM-5 and Al_2O_3. Furthermore, images were acquired by the mean of high-resolution transmission electron microscopy (HRTEM) using a Thermo Scientific Talos F200X microscope operated at 200 kV, equipped with a detector for energy dispersive X-ray spectroscopy (EDX). The sample powder was suspended in high-purity 2-propanol and then dripped on the lacey carbon film of a gold support grid. EDX maps in scanning-transmission mode (STEM) were collected to investigate the elemental distribution.

The strength of the basic sites of the prepared samples was determined by CO_2-TPD. The analyses were carried out in an Altamira AMI-300Lite Chemisorption Analyzer. Approximately 50 mg of catalyst powder was placed in a quartz reactor, between two quartz wool layers, and it was pre-treated at 500 °C for 2 h in He flow. Then, the catalyst surface was saturated by flowing 20 mL/min of pure CO_2 at RT for 30 min. After purging the physisorbed CO_2 with a stream of He (30 min at 50 °C), the desorption step was performed by heating the sample up to 800 °C with a 10 °C/min ramp under a 20 mL/min stream of He. The same instrument was employed to perform H_2 temperature programmed reduction (H_2-TPR) analyses. 50 mg of sample were pre-treated in a He stream with a heating ramp (500 °C, 10 °C/min). After 60 min at 500 °C, the reactor was cooled in a stream of He. The sample was then heated from 50 up to 800 °C with a 10 °C/min ramp, while flowing 20 mL/min of 5% H_2 in He.

Fourier transform infrared spectroscopy (FTIR) was carried out by using a Bruker Invenio S spectrometer equipped with an MCT detector. Spectra of Ru-functionalized catalysts were recorded in transmittance mode in the region ranging from 4000 to 800 cm^{-1} at a spectral resolution of 2 cm^{-1}. The samples were pressed at 5 tons to obtain a thin tablet and embedded within a quartz IR cell equipped with KBr optical windows. Firstly, a room-temperature spectrum was acquired; thereafter, each sample was degassed at 10^{-4} mbar and treated at 500 °C (heating ramp 5 °C/min) for 1 h by connecting the IR cell to a high vacuum line. The material surfaces were reduced dosing 20 mbar of pure H_2 during the thermal treatment. Subsequently, the system was cooled to room temperature and spectra were collected at beam temperature (R.T.) by dosing increasing amounts of CO_2 (from 1.5 $\times 10^{-3}$ to 25.0 mbar equilibrium pressure range) on samples. Since CO_2 is an acid probe, this experiment enables to study the basic sites, because of the formation of carbonate-like species characterized by typical IR bands in the 1700–1200 cm^{-1} range [50–52].

The CO_2 adsorption measurements were performed employing an experimental set-up consisting of a reactor with a fixed adsorbent bed, a furnace, and a gas analyzer. In this system, the catalyst was placed in a quartz U-shape reactor with a sintered glass sector. The reactor located in a Lenton® Tube Furnace (LTF) was connected to the inlet gas through a stainless-steel tube with an outer diameter (O.D.) of 1/4". A HARTMANN & BRAUN® Advance Optima gas analyzer devoted to measuring different gas components quantified the CO_2 volume fraction expressed in % v/v in the outlet gas every 10 s. A K-type thermocouple monitored the reactor temperature during the process. A Bronkhorst® mass flow controller regulated the gas inlet flow rate.

Adsorption tests were carried out using a mixture of 8 vol% CO_2 in N_2 (assuming the flue gas composition) in three temperature conditions of 150, 200, and 250 °C in order to evaluate the performances of all six materials incrementing the temperature. Before the adsorption tests, 300 mg of catalyst were pelletized (500–250 μm), crushed, and sieved, and loaded into the U-shaped reactor. Initially, the materials were pretreated at 500 °C for 2 h in N_2 flow, then the system was cooled down to reach the experimental temperature. The total flow of the gas mixture used was 40 mL/min. For each adsorption experiment, the materials were left in an atmosphere of 8% CO_2/ N_2 for 30 min. During the adsorption experiments, the CO_2 volume fraction in the outlet gas was recorded with the gas analyser until the concentration of the analysed gas at the inlet of the reactor and outlet of the analyser became equal. In each adsorption experiment the adsorbed amount of CO_2 was calculated using the following equation:

$$q_{CO_2 adsorbed}\left(\mu mol \quad g^{-1}\right) = \frac{\dot{Q}_{in}\frac{P}{RT} \quad \int_{t_0+\Delta t}^{t_f}\left(\frac{y_{CO_2,in}-y_{CO_2,out}}{1-y_{CO_2,out}}\right)dt}{m_{sorbent}} \quad (3)$$

where $\dot{Q}_{in}$ is the total inlet flow rate, $y_{CO_2,in}$ represents the mole fraction of CO_2 in the inlet recorded by gas analyser at the beginning of each experiment, $y_{CO_2,out}$ is the mole fraction of the CO_2 in the outlet, $\Delta t(s)$ is the assumed delay time of gas analyser measurement, and m is the weight of the sorbent. In this equation, the temperature values are the following: 150, 200 and 250 °C. The operating pressure is 1 atm. More details on the derivation of Eq. (3) are given in the supporting information file.

Methanation tests were conducted in a gas implant equipped with an EMERSON X-STREAM XE gas analyser, provided with the following channels: a nondispersive infrared detector for CO, CO_2, and CH_4, a thermal conductivity detector for H_2, and a paramagnetic sensor for O_2. 400 mg of sample were pre-treated in N_2 flow (500 °C, 150 mL/min) and then in a stream of 5% H_2 in N_2 (500 °C, 150 mL/min) for a total of 2 h. Therefore, the reactor was cooled to 250 °C, temperature chosen for the subsequent steps, and purged with a stream of N_2 for 30 min. After the stabilization of the temperature, a stream of 8% CO_2 in N_2 was sent to the reactor (250 °C, 150 mL/min, for 30 min), and, after a second purge with N_2 (30 min), the CO_2 adsorbed was converted to methane by sending another gas mixture of 5% H_2 in N_2 to the material (250 °C, 150 mL/min, for 30 min). In order to study the stability of the materials, cyclic experiments were performed, simulating a continuous work of the material.

The amount of CO_2 adsorbed in each methanation test was calculated with the previous Eq. (3). As regards the quantification of the methane produced, it was carried out through Eq. (4):

$$\hat{n}_{CH_4,prod}\left(\mu mol \quad g^{-1}\right) = \frac{\dot{Q}_{in}\frac{P}{RT} \quad \int_{t_0+\Delta t}^{t_f}\left(\frac{y_{CH_4,out}}{1+y_{CH_4,out}}\right)dt}{m_{sorbent}} \tag{4}$$

where $\dot{Q}_{in}$ state for the total inlet flow rate, $y_{CH_4,out}$ is the mole fraction of the CH_4 in the outlet, $\Delta t(s)$ is the assumed delay time of gas analyser measurement, and m is the weight of the catalyst. Further details on the derivation of Eq. (4) are given in the supporting information file.

The yield of the reaction was estimated through Eq. (5).

$$Y_{CH_4}(\%) = \frac{\mu mol_{CH_4out}}{\mu mol_{CO_2adsorbed} - \mu mol_{CO_2desorbed}} \times 100 \tag{5}$$

In the process yield calculation, the amount of methane produced is divided by the quantity of CO_2 adsorbed minus the amounts CO_2 physisorbed, which was desorbed during the purge step and did not take part in the catalytic reaction.

3. Results and discussion

3.1. Structural, textural, and physico-chemical properties

In order to verify that the synthesis by impregnation was successful, the cerium and ruthenium contents loaded on the two supports were determined by ICP-MS. The values obtained are summarised in Table 1 and are in agreement with the nominal quantity calculated to perform the impregnation. Small discrepancies between nominal and experimental values can be attributed to the instrumental accuracy of the ICP-MS.

By the mean of X-ray diffraction, it was possible to investigate the crystalline phases of the catalysts. All the relevant peaks in the diffractograms were identified by using the PDF-2 Release 2004 database. In Fig. 1, the diffractograms of ceria-based materials impregnated on Al_2O_3 and ZSM-5 supports are compared with the patterns of bare CeO_2, Al_2O_3 and ZSM-5, and with those of the two Ru-functionalized catalysts. Typical fluorite crystal structure characterizes the pattern of pure cerium oxide, consisting of eight signals [53]. Aluminium oxide support shows the characteristic pattern of γ-phase, while the zeolite support exhibits the typical MFI framework pattern. All the mixed materials are characterized by the specific peaks of ceria, namely at 29° (111), 33° (200), 47° (220), 56° (311), 59° (222), 69° (400), 76° (331) and 79° (420), while the other reflections refer to the support fingerprints. As expected, an increase in the intensity of the reflections relative to the cerium oxide is observed as the percentage of precursor used in the preparation of the material increases. This suggests a greater coverage of the supports by the impregnation procedures, confirmed by the decrease in the intensity of the reflections relative to the two supports. Clearly, the peaks referred to ceria are more resolved in the regions of the diffractograms uncontaminated by reflection of the two supports, namely below 35°, from 50° to 65°, and above 70° in the case of Al_2O_3--supported materials. Since the MFI pattern of ZSM-5 is rich of peaks, the presence of ceria is pointed out by asymmetrical and enlarged signals, which become more intense and evident in the 30% loaded sample. The diffractograms of 2R30CA and 2R30CZ were collected after a reduction treatment (performed in a stream of 5% H_2 in N_2). It is possible to observe the more intense crystallographic reflections associated to the presence of metallic Ru, namely at 38.4° (010) and 44° (011). In Table 2 the mean crystallite sizes of the crystal phases calculated through Scherrer's equation are reported. Generally, the cerium oxide crystallites present an average size between 6.0 and 6.8 nm. Ceria phase on zeolite support is characterized by larger crystallites, depicted by sharper XRD peaks. Concerning the metallic ruthenium phase, in 2R30CA the distinctive peaks reveal crystallites with an average size around 15 nm (broad signals), while in 2R30CZ the peaks are sharper, evidence of larger crystallite sizes (ca. 30 nm).

In Fig. S1 the N_2 physisorption plots are reported for all samples. According to the IUPAC assignation [54], the zeolite-supported materials show isotherms ascribable to type Ia. This kind of isotherms is typical of microporous adsorbents; indeed, the extent of coating by cerium oxide on the support is low and therefore the materials behave like a pure microporous zeolite. The drop of micropore volume (Table 2) confirms the coating of the zeolite surface by the cerium phase. The little hysteresis loop is due to the long-range mesoporous behaviour of the interparticle voids of the zeolite.

Regarding the other samples (aluminium oxide-supported ones), their isotherms can be ascribed to type IVa, characteristic of mesoporous materials. The adsorption behaviour in mesopores is governed by the adsorbent-adsorbate interactions and by the interactions among the molecules in the condensed state. The presence of the loop suggests that capillary condensation is accompanied by hysteresis. These materials exhibit a hysteresis loop of H3-type, respectively in the 0.45–0.90 p/p^0 range for zeolite-supported samples (section **A**) and the 0.60–0.90 p/p^0 range for aluminium oxide-supported samples (section **B**). Section **C** refers to the samples impregnated with ruthenium, 2R30CZ and 2R30CA. The increase in the mass percentage of ceria deposited on the support leads to a decrease in the specific surface area (Table 2), for both zeolite and aluminium oxide supports. This fact confirms that cerium oxide covers the surface of the supports. The specific surface area further decreases appreciably for both samples impregnated with ruthenium, even if the Ru percentage by weight is relatively low. Pore width distributions of supported materials and Ru-ceria supported catalysts are depicted in Fig. S2 in the supporting information file.

The surface chemistry of the various catalysts was studied by the mean of XPS. The deconvoluted spectrum of Ce 3d level (Fig. 2, section **A** and **B**) offers two multiplets, namely v and u, that correspond to the spin-orbit split $3d_{5/2}$ and $3d_{3/2}$ core holes. The intensity ratio I $3d_{5/2}$/I $3d_{3/2}$ was fixed to 1.5. The pair of spin-orbit doublets generates ten peaks which characterize the CeO_2 XP spectrum in agreement with other authors [55–58]. The u''' and v''' peaks, corresponding to the highest binding energy, are located at about 916 and 898 eV and are the result of

Table 1
Summary of the materials prepared with the corresponding CeO_2 and Ru loading.

Sample	Nominal Ru wt%	Nominal CeO_2 wt%	CeO_2 wt%[a]	Ru wt%[a]
10CZ	–	10	7.6	–
20CZ	–	20	18.7	–
30CZ	–	30	30.7	–
10CA	–	10	8.2	–
20CA	–	20	19.4	–
30CA	–	30	30.2	–
2R30CZ	2	30	31.0	1.8
2R30CA	2	30	29.4	2.1

[a] Inductively coupled plasma Mass Spectrometry (ICP-MS)

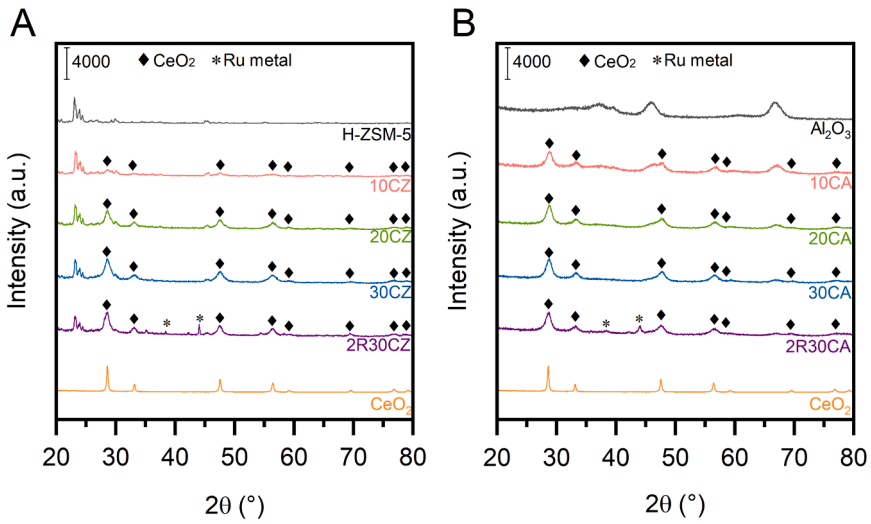

Fig. 1. XRD diffractograms of **A)** aluminium oxide-supported materials and **B)** zeolite-supported ones. The patterns of pure γ-Al_2O_3, CeO_2 and H-ZSM-5 are also depicted. Since several reflections are present, the peaks of CeO_2 (◆) and metallic ruthenium (*) are highlighted.

Table 2
Summary of the structural and textural properties of the catalysts derived from XRD, N_2 adsorption-desorption and XPS analyses.

Sample	D (nm)[a]	SSA (m^2/g)[b]	Pore Volume (cm^3/g)[c]	Average pore width (nm)[c]	Micropore Volume (cm^3/g)[c]	Cerium species (%)[e]	Ce^{3+}/Ce^{4+} ratio[e]	Ru species (%)[e]	Oxygen species (%)[e]
H-ZSM-5	——	288	0.16	2.4	0.123	——	—	——	72 (O_α) 28 (O_β)
10CZ	6.2	270	0.18	2.7	0.096	56 (4 +) 44 (3 +)	0.79	——	87 (O_α) 13 (O_β)
20CZ	6.0	267	0.21	2.9	0.090	56 (4 +) 44 (3 +)	0.79	——	75 (O_α) 25 (O_β)
30CZ	6.0	229	0.21	3.6	0.074	57 (4 +) 43 (3 +)	0.75	——	58 (O_α) 42 (O_β)
2R30CZ	30 (Ru)	187	0.17	3.7	0.071	60 (4 +) 40 (3 +)	0.67	Ru^0 (37%) Ru^{4+} (42%) Ru^{n+} (21%)	24 (O_α) 76 (O_β)
γ-Al_2O_3	——	200	0.21	5.4	——	——	——	——	40 (O_α) 60 (O_β)
10CA	6.8	192	0.48	10.5	——	59 (4 +) 41 (3 +)	0.69	——	38 (O_α) 62 (O_β)
20CA	6.7	183	0.44	10.0	——	60 (4 +) 40 (3 +)	0.67	——	34 (O_α) 66 (O_β)
30CA	6.3	150	0.34	9.4	——	60 (4 +) 40 (3 +)	0.67		35 (O_α) 65 (O_β)
2R30CA	15.3 (Ru)	130	0.29	8.7	——	59 (4 +) 41 (3 +)	0.69	Ru^0 (26%) Ru^{4+} (41%) Ru^{n+} (33%)	33 (O_α) 67 (O_β)

[a]XRD analysis;
[b]Calculated according to Brunauer-Emmett-Teller (BET) method;
[c]Calculated according to Barrett-Joyner-Halenda (BJH) algorithm;
[d]Calculated according to the t-plot method;
[e]XPS surface measurements.

Ce $3d^94f^0$ O $2p^6$ final state. It is possible to ascertain the presence of tetravalent Ce (Ce^{4+} ions) thanks to the characteristic satellite peak u''' associated to the Ce $3d_{3/2}$. The lowest binding energy states u, v, u'', v'' (901, 882, 907, and 888 eV) are the result of Ce $3d^94f^2$ O $2p^4$ and Ce $3d^94f^1$ O $2p^5$ final states. After the spectrum deconvolution, the presence of Ce (III) could be identified thanks to the existence of u' and v' peaks, respectively at about 903 and 885 eV, which are ascribed to the Ce $3d^94f^1$ O $2p^6$ final state. The less intense u^0 and v^0 signals, incorporated in the multiplets at 898.9 and 880.2 eV respectively, are also ascribed to Ce (III) [59,60]. The deconvoluted Ce 3d spectra of the Ru-functionalized catalysts are depicted in Fig. S3.

Ru $3d_{5/2}$ and $3d_{3/2}$ peaks, below 284 eV and above 284 eV respectively, were used to study the oxidation states of Ru, despite an overlapping with C 1 s signals at 284.8 and 288.8 eV (Fig. 3, section **C**). The peaks at around 280, 281, and 282 eV can be assigned to Ru^0, Ru^{4+} (crystalline RuO_2, or RuO_2 thin layers), and cationic ruthenium species (Ru^{n+}, with $4 \leq n \leq 6$), respectively, for both the Ru-loaded catalysts [61]. These latter species, characterized by higher positive charge density, could be attributed to Ru cations diffused into CeO_2 lattice, possibly substituting a Ce^{4+} ion [62]. Guo *et al.* [63] observed that Ru species in cerium oxide support exhibit a more intense electronic interaction compared to metal nanoclusters and nanoparticles. This condition could produce a peak shift associated to Ru^{n+} in the form of Ru-O-Ce bond over the oxide surface or at the $RuO_x - CeO_2$ interface via electron transfer [64].

The semi-quantitative composition of the outer atomic layer of the composite materials is reported in Table 2**.** The areas under the peaks of Ru 3d spectra were quantified in order to calculate approximately the

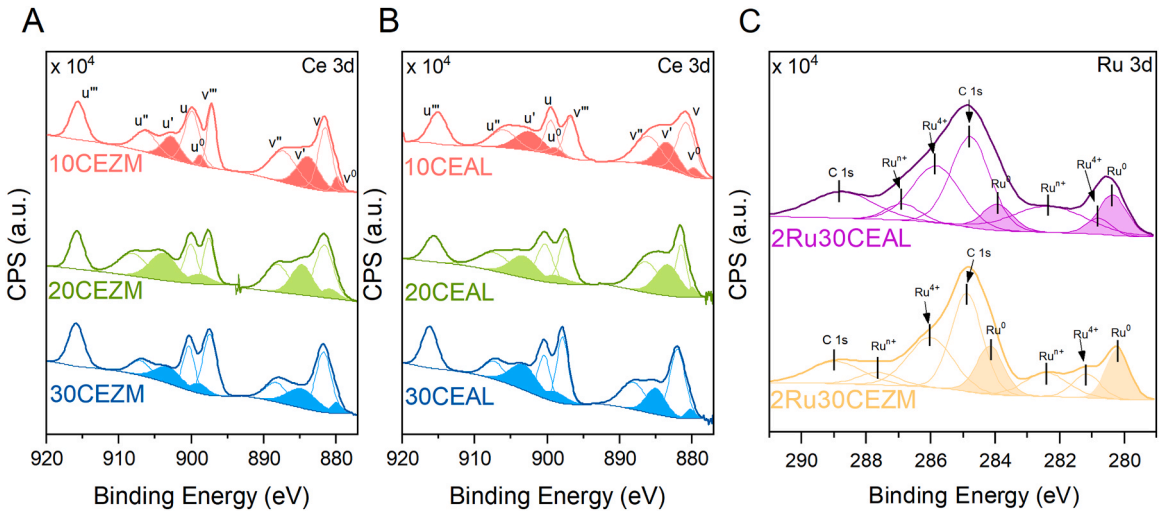

Fig. 2. **A)** Ce 3d XP spectra of zeolite-supported materials and **B)** alumina-supported ones. **C)** Ru 3d XP spectra of the two ruthenium functionalized catalysts.

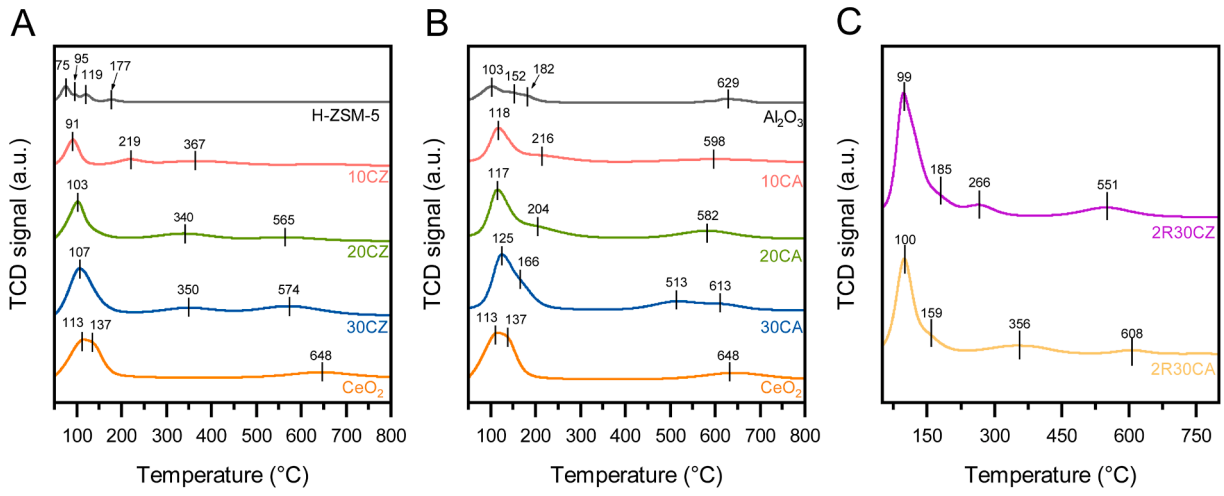

Fig. 3. CO_2-TPD profiles of **A)** the xCZ and **B)** xCA materials compared with pure ceria, H-ZSM-5 and Al_2O_3. **C)** CO_2-TPD profiles of Ru-functionalized catalysts.

proportion of ruthenium species and the percentages are summarized in Table 2. From the semi-quantitative analysis of the areas, 2Ru30CA seems to possess more Ru^{n+} species, which indicates greater metal support interaction between Ru and Ce, compared to the zeolite supported sample.

Information about the surface oxygen species of the catalysts can be provided analysing the O 1s XP spectra (Fig. S4). All Al_2O_3-supported samples show the same broad peak centred at around 531 eV containing more than one signal arising from the overlapping contribution of the chemical oxygen species bounded to cerium. Two contributions can be supposed and distinguished from a deconvolution procedure. The broader signal could be ascribed to lattice oxygens (~530 eV), namely O^{2-} ions bounded to cerium (O_β), while surface oxygens (O_α) and hydroxylic groups (–OH) and/or surface adsorbed oxygen molecules (O_2) have their peak at around 531 eV [55,65,66].

Conversely, ceria-zeolite materials exhibit two distinct peaks, one at 528.8 eV, and the second at ca. 531 eV. The one at lower binding energies could be attributable once more to bulk CeO_2 oxygen, while the signal above 531 eV could be related to the surface oxygen species of the oxide together with the oxygen species of the zeolite support [49,67]. The intensity of the signal associated to ceria lattice oxygen rises with the increase in the amount of impregnated Ce.

The quantity and the type of basic sites were investigated by the mean of CO_2-TPD: the recorded profiles are displayed in Fig. 3, while the quantity of CO_2 released is reported in Table 3. Generally, desorption peaks at low (< 200 °C), medium (200–500 °C) and high temperature (> 500 °C) can be ascribed to the presence of weak, moderate, and strong basic sites, respectively [68,69]. Indeed, metal oxides can adsorb CO_2 on basic sites with various strength thanks to the presence of superficial OH, O^{2-} or cations, entailing the creation of several carbonaceous species, i.e., hydrogen carbonates, mono/bi/polydentate

Table 3
Quantitative evaluations determined from the CO_2-TPD.

Sample	Weak basic sites	Medium basic sites	Strong basic sites
	$\mu mol_{CO_2} g^{-1}$		
CeO_2	230	175	77
Al_2O_3	47	95	1
ZSM-5	72	40	53
10CZ	144	131	30
20CZ	266	138	43
30CZ	286	133	164
10CA	126	93	46
20CA	243	37	124
30CA	310	17	161
2R30CZ	309	84	199
2R30CA	299	134	48

carbonates or metal carboxylates [55,70]. In Fig. 3, the intense desorption peaks below 200 °C are probably due to the decomposition of several less stable CO_2 species, such as monodentate carbonates. The other large bands from 200 °C to 500 °C could be ascribed to the presence of more stable bidentate and polydentate carbonates. Finally, carbonates strongly adsorbed on the basic sites contribute to the signals at higher temperatures [55,68]. As reported in Table 3, the amount of CO_2 desorbed for the as-prepared materials rises as the ceria content increases. All the samples show a pronounced desorption peak below 150 °C, demonstrating that most of the CO_2 chemisorbed on the surface of the catalysts binds to weak basic sites. This desorption peak can be clearly observed in commercial cerium oxide, which exhibits a desorption profile characterised above all by a conspicuous quantity of CO_2 released below 200 °C. The ZSM-5 and Al_2O_3 substrates also exhibit weak basic sites that contribute to the same desorption peak of the as-prepared samples. For both supports, the highest desorption values were achieved by the samples functionalised by 30% CeO_2, i.e., 30CZ and 30CA, which desorbed 583 $\mu mol_{CO2}\ g^{-1}$ and 488 $\mu mol_{CO2}\ g^{-1}$ of CO_2, respectively.

Looking at the desorption values of the three different types of sites, it can be seen that the site strength is linked to the type of support. For the samples supported on zeolite, the amount of medium and strong basic sites corresponds to more than 50% of the total number of sites on the catalysts surface. On the other hand, the same sites are less than half for the samples supported on alumina. It is possible that the different interaction between ceria and zeolite may favour the generation of stronger binding sites, which cause a higher uptake of CO_2, as observed in adsorption tests (*Section 3.2.1*).

In Fig. 3 ***C***, the CO_2-TPD plots of the Ru-loaded samples are depicted. 2R30CZ resulted in a total desorption of 592 $\mu mol_{CO2}\ g^{-1}$, while 2R30CA desorbed a total of 481 $\mu mol_{CO2}\ g^{-1}$. These values are almost equal to those of the corresponding 30CZ and 30CA samples, indicating that Ru addition has no evident effects on CO_2 adsorption capacity. Even in this case, the gap between the two catalysts could be ascribed to different interactions between ceria and the supports which caused distinct dispersions, as confirmed by TEM analysis and further discussed in *Section 3.2.1* .

H_2-TPR was carried out on pure ceria, the ceria-based materials, and the Ru-functionalized catalysts; the collected profiles, in terms of TCD signal as a function of temperature up to 800 °C, are plotted in Fig. 4. According to the literature [71–75], cerium oxide is reduced by H_2 only at temperatures higher than 400 °C and two reduction peaks correspond to the reduction of superficial cerium (here at about 480 °C) and bulk CeO_2 above 800 °C (not visible in Fig. 4). By integrating the TPR signals between 200 °C and 800 °C, the H_2 consumption was estimated, and the values are reported in Table 3. For pure CeO_2 a H_2 uptake of 743 $\mu mol_{H2}\ g^{-1}$ was obtained, corresponding to the reduction of 26% of cerium in the whole sample from the oxidation state 4 + to 3 + . The effect of the two supports is visible in the shift towards lower temperature of the reduction peak of ceria surface, together with a higher hydrogen consumption (exceeding the 60% of the theoretical maximum consumption for 30CZ and 30CA, see Table 3); this indicates that the reduction of ceria is promoted when it is dispersed over high surface area zeolite (30CZ) and alumina (30CA). Typically, ZSM-5 zeolite does not exhibit reduction peaks [76]; however the shift and different shape of the reduction peak at 399 °C could be also ascribed to the strong interaction between CeO_2 and ZSM-5 [77]. Similarly, for the sample supported on alumina, a wide peak centred at 397 °C is observed; in this instance, the interaction between ceria and the support can lead to the formation of $CeAlO_3$ species, which increase the surface reducibility of CeO_2 [78].

According to Fig. 4 ***B***, Ru species in the functionalized composite materials are reduced below 200 °C. The 2R30CZ sample exhibits two signals: a sharp reduction peak at low temperature, centred at 150 °C and a weak shoulder at 193 °C. This profile suggests the presence of two types of Ru species, one more abundant than the other. 2R30CA is characterized by two sharp peaks at 137 °C and 180 °C, and, again, the presence of multiple signals could indicate the existence of different ruthenium species. Some authors indeed observed a correspondence between lower reduction temperature and well-dispersed RuO_x species, strongly interacting with CeO_2 surface; instead, RuO_2 phases with a high grade of crystallinity could be reduced at a moderately higher temperature, since these species weakly interact with the CeO_2 support [64,79]. In Fig. 4 ***B***, the typical peak of CeO_2 surface reduction (around 390 – 400 °C) is also visible for both the Ru-containing catalysts, and it is centred at the same temperature observed for the composite materials prior to Ru functionalization. The H_2 quantity consumed at low and high temperature during the TPR was quantified for each catalyst, and the values are included in Table 4. As demonstrated by the comparison between the measured observations and the theoretical values, the hydrogen consumption for 2Ru30CZ at low temperature slightly exceeds the theoretical $\mu mol\ g^{-1}$ of H_2 necessary for the complete reduction of Ru species. This indicates that some neighbouring Ce ions are reduced concurrently, suggesting that a significant metal-support interaction is established between ruthenium species and ceria [80,81]. RuO_x species strongly interacting with cerium oxide, once reduced to Ru^0, can indeed enhance H_2 dissociation and promote the reduction of CeO_2 surface at

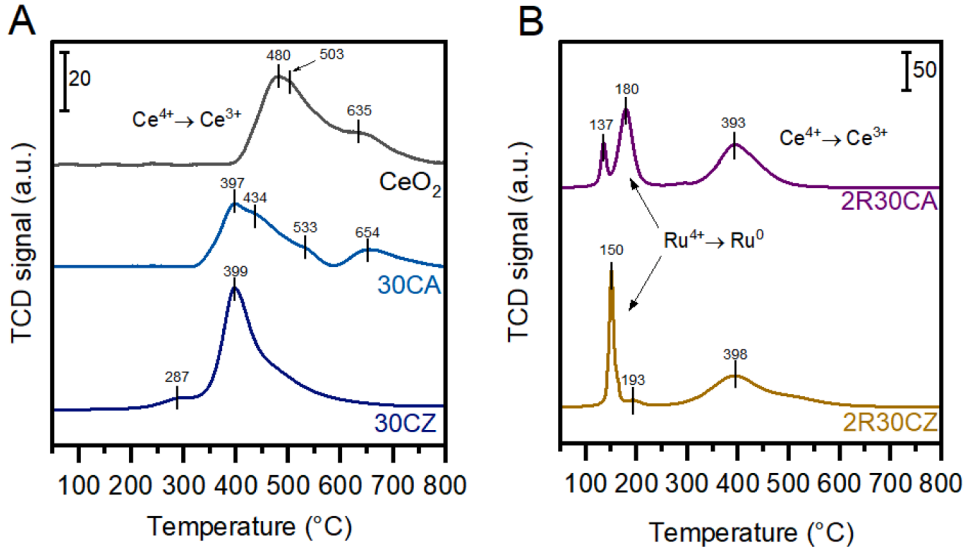

Fig. 4. H_2-TPR profiles of **A)** the 30CZ and 30CA materials compared with pure ceria. **B)** H_2-TPR profiles of Ru-functionalized catalysts.

Table 4
Quantitative evaluations determined from the H_2-TPR.

Sample	$Ru^{4+} \rightarrow Ru^0$	$Ce^{4+} \rightarrow Ce^{3+}$	$Ru^{4+} \rightarrow Ru^0$	$Ce^{4+} \rightarrow Ce^{3+}$
	$\mu mol_{H_2}\ g^{-1}$			
	Measured consumption		Theoretical consumption	
CeO_2	—	743	—	2907
30CZ	—	528	—	892
30CA	—	536	—	878
2R30CZ	348	506	271	901
2R30CA	399	501	315	855

lower temperature [79,82]. Concluding, both 2R30CA and 2R30CZ are characterized by a molar ratio between consumed H_2 and Ru of 2.5 and 2.6, respectively, which are values only slightly higher than the stoichiometric one (i.e., 2). This implies that no significant consumption of hydrogen for ceria reduction could be expected during cyclic methanation.

The morphology of the ruthenium-functionalized catalysts was investigated via electron microscopy, both in scanning and transmission modes. As shown in Fig. S5, the surfaces of the materials are particularly disordered and different from each other. 2R30CZ shows a relatively smooth surface, far away from the coral-like surface exhibited by 2R30CA. These morphologies are the result of the synthetic route used to prepare the samples; actually, impregnation does not allow the formation of geometrically organised structures but offers the possibility of adequate dispersion of the species on the surface of the supports. By the mean of HRTEM technique, the distribution of cerium oxide and ruthenium species was observed. In Fig. 5 the STEM images together with EDX maps for Ce and Ru are depicted. Ceria covers all the support surface for both 2R30CA (section **A**) and 2R30CZ (section **B**). Instead, due to its low weight percentage, Ru is not evenly dispersed over the surface, but rather aggregated in small clusters around 10 nm in size, as shown in the two maps. As depicted in Fig. S6, 2R30CZ possesses areas where only a well-dispersed ceria phase is present; this feature could enhance the ceria surface available for the CO_2 adsorption but the absence of Ru interacting with CeO_2 could be the reason for this catalyst's lower methanation activity in some areas of the sample (see *Sections 3.2.1* and *3.2.2*).

Fig. 6 A reports the FT-IR spectra of the samples outgassed at 500 °C and then exposed to hydrogen atmosphere (20 mbar) before dosing CO_2. To allow a clearer analysis between the two materials, all the depicted spectra were normalized to the unit specific weight. The two spectra are characterized by the signals belonging to cerium oxide together with their respective supports, namely zeolite ZSM-5 and aluminium oxide. Concerning the zeolite-supported catalyst, in the OH stretching region (3800–3000 cm^{-1}) the signals of the support and the CeO_2 are overlapped. According to the literature, the following peaks can be assigned to the zeolite support: silanol hydroxyls (~3743 and ~3663 cm^{-1}), Brønsted acid hydroxyls (~3590 cm^{-1}) and the broad band at around 3474 cm^{-1} generally ascribed to hydroxyl nests involving several silanol groups interacting through extended hydrogen bonding [83,84]. Cerium oxide hydroxyl signals can be distinguished in the two catalysts as follow: isolated hydroxyls (3710–3700 cm^{-1}), bridging hydroxyls (3660–3640 cm^{-1}), multiple bonded hydroxyls (3550–3500 cm^{-1}) and hydrogen bridging hydroxyls (broad band at 3400–3100 cm^{-1}) [85]. It is challenging to distinguish between Ce^{4+} and Ce^{3+} species without any probe molecule. Some authors identified the presence of reduced Ce species due to the weak signal at around 2130 cm^{-1} linked to the $^2F_{5/2}$ - $^2F_{7/2}$ electronic transition of reduced ceria in bulk defective sites [50,86,87]. Furthermore, Badri *et al.* found that the different oxidation states of cerium generate two signals with different wavenumbers in the hydroxyl region, i.e., the former at around 3635 cm^{-1} attributable to Ce^{4+} and the latter at around 3647 cm^{-1} ascribable to the presence of Ce^{3+} [88]. At lower wavenumbers, all spectra exhibit signals at 2930 and 2840 cm^{-1} relating to C-H stretching vibrations of formate species [85]. Moreover, the bands in the 1800–1000 cm^{-1} range can be readily assigned to C-O stretching and bending modes of carbonate and formate species. The zeolite-supported catalyst displays the typical ZSM-5 IR spectral features [83]. Infrared spectra of the two catalysts were collected at room temperature while dosing increasing pressures of CO_2 gas from 1.5×10^{-3} to 25 mbar in order to investigate the nature of carbonaceous species generating by CO_2 adsorption. Fig. 6 ***B*** and ***C*** depict the wavenumbers

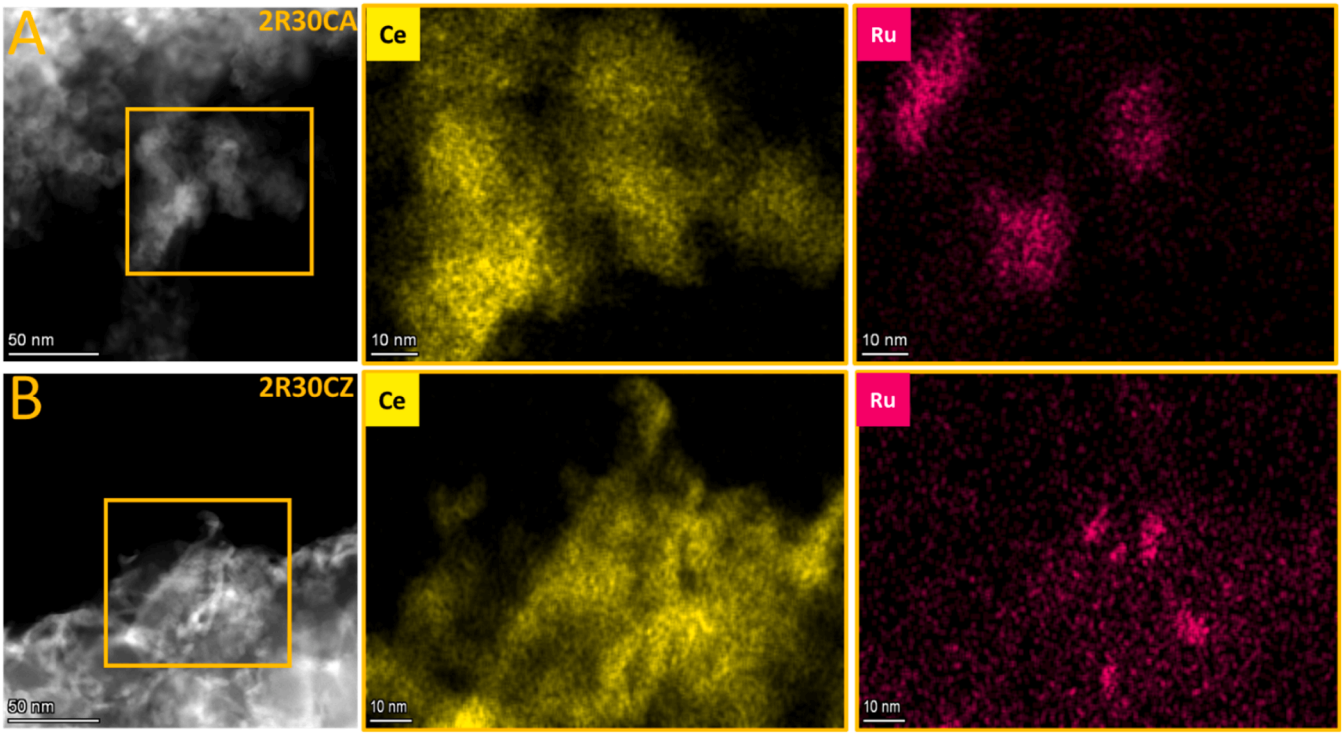

Fig. 5. STEM images of **A)** 2R30CA and **B)** 2R30CZ Ru-functionalized catalysts and associated EDX maps indicative of cerium and ruthenium distribution.

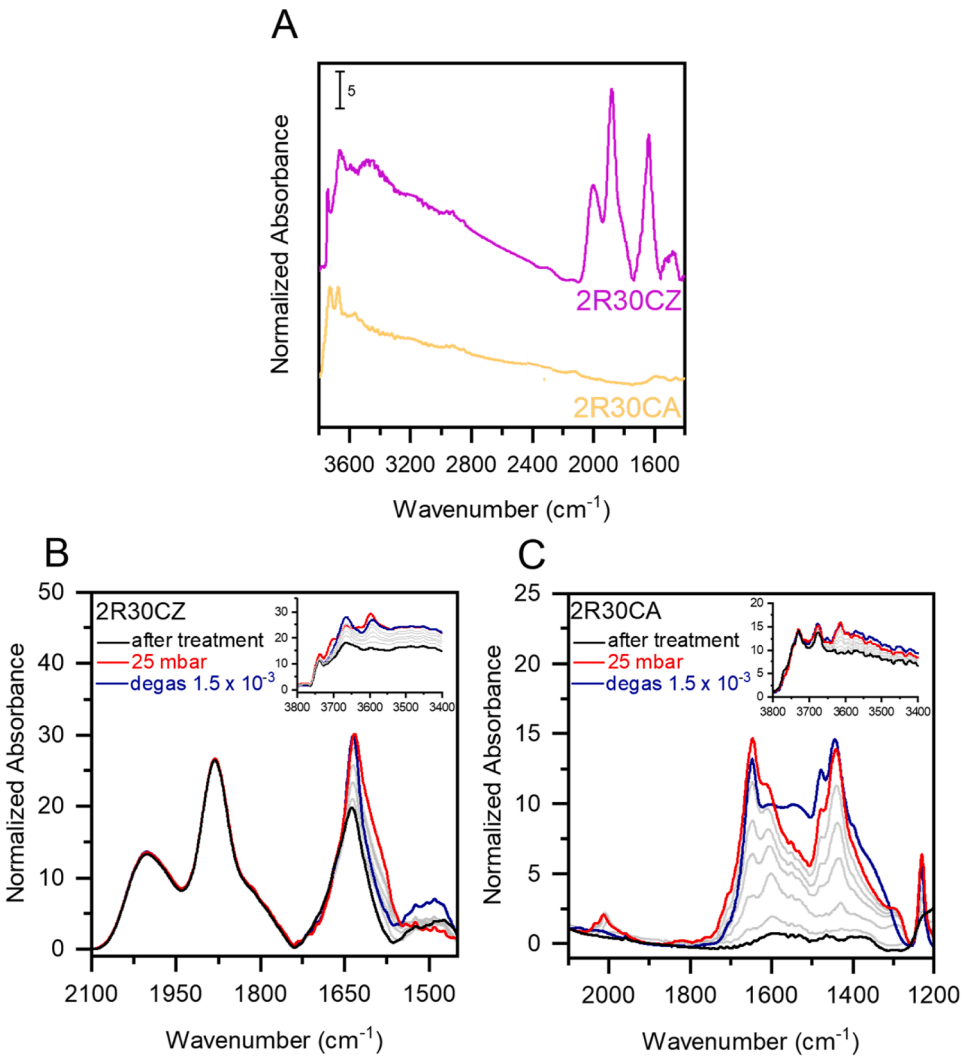

Fig. 6. In situ FT-IR spectra of CO_2 adsorbed at increasing equilibrium pressure (from 1.5 $\times 10^{-3}$ to 25 mbar). **A)** FT-IR spectra of 2R30CZ and 2R30CA after the pretreatment and collected on the **B)** 2R30CZ and **C)** 2R30CA samples during CO_2 adsorption. Bold curves in sections **A**, **B** and **C** refer to spectra taken after reductive treatment (black), at a CO_2 equilibrium pressure corresponding to ca. 25 mbar (red) and after subsequently degassing at 1.5 $\times$ 10^{-3} mbar (blue). The inset shows enlarged hydroxyl spectral region.

range 2200–1200 cm^{-1} along with the hydroxyl stretching region reported in the inset. For the sake of clarity, the types of species observed in the infrared spectra are shown with their corresponding wavenumber assignments in Scheme 1. At 25 mbar equilibrium pressure (red line) different types of carbonates and bicarbonates are formed in the region ^{1}640–1550 cm^{-1}. The signal centred at ~1590 cm^{-1} can be ascribed to bidentate carbonates; the wide shoulder comprised between 1610 and 1550 cm^{-1} can be readily assigned to carboxylate species [85,89]. An outgassing procedure up to1.5 $\times$ 10^{-3} was performed at the end of the entire FT-IR experiment (obtaining the blue spectra shown in Fig. 6). Generally, it is possible to notice that the contribution of carboxylate species decreases while a new signal centred at around 1490 cm^{-1} rises. This behaviour could be related to the disappearance of less stable ionic species (carboxylates) and the appearance of more stable polydentate species. The spectra in the range 3800–3400 cm^{-1} portrayed in the insert show a meaningful rise of the OH stretching signals linked to several typologies of carbonates species [90,91]. The range 2200–1200 cm^{-1} of 2R30CA (section ***C***) is characterized by several overlapped contributions: bridge bidentate carbonate species (~1710 and ~1294 cm^{-1}), bidentate chelate carbonates (~1645 cm^{-1}), polydentate carbonates (~1480 cm^{-1}), monodentate carbonates (~1440 and 1230 cm^{-1}) [85]. The shoulder at 1298 cm^{-1} could indicate the presence of different configurations of linkage such as bridge bidentate carbonate and/or bidentate chelate carbonate [46,90,91]. The broad spectral feature noted in the range 2100–1900 cm^{-1} which is characterized by a maximum at 2010 cm^{-1} and an asymmetric tail at lower frequencies, may contain contributions from several adsorbed CO species due to activated adsorption of CO on Ru [92–94]. Panagiotopoulou *et al.* attributed this band to mono carbonyl species adsorbed on partially oxidized Ru sites (Ru^{n+}-CO, with n < 4). The low-frequency tail of this signal suggests the existence of (CeO_2)-Ru-CO species at the metal-support interface [95]. The latter signal disappears through the outgassing step because of its weakness. This procedure results in a slight modification of the final spectrum which keeps on being featured by several carbonaceous species. The spectra in the range 3800–3400 cm^{-1} depicted in the insert do not display meaningful signals. The peak at ~3672 cm^{-1} can be associated with the $\nu(OH)$ modes of newly formed hydroxyl groups of the bicarbonates. The intensity of these groups correlates with the rise of the signal of monodentate bicarbonates; whereas the peak at 3611 cm^{-1} could be ascribed to the bidentate chelate bicarbonate. Lastly, the broad features below 3580 cm^{-1} could be owing to the interaction between the hydroxyl groups of the formed bicarbonates [90]. Then, it is possible to confirm the results obtained from the CO_2 desorption profiles (Table 3),

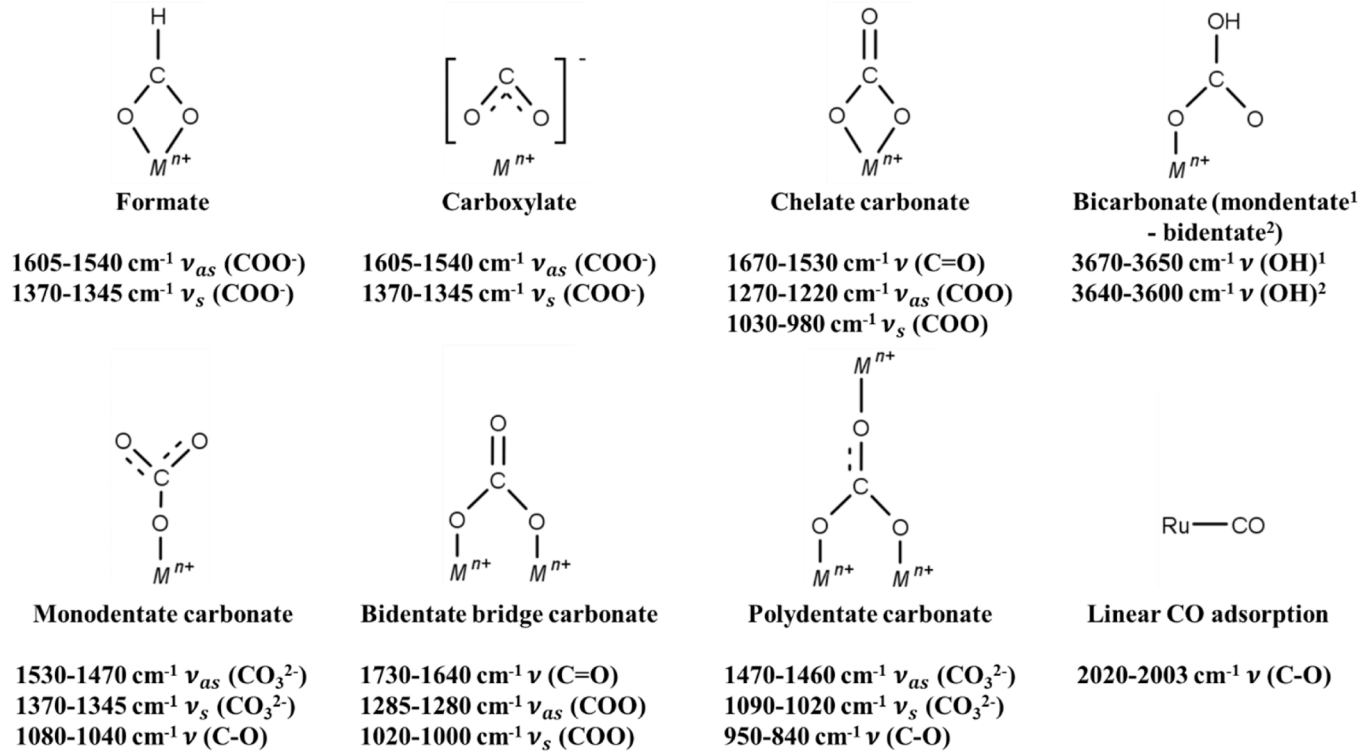

Scheme 1. Types and wavenumber assignments of formate and carbonate-carboxylate species on ruthenium-ceria-zeolite/alumina catalysts.

observing the formation of carbonyl species strongly linked to the basic sites of ceria.

3.2. Adsorption and catalytic results

3.2.1. Adsorption breakthrough curves

Several studies have been focused on the interaction of CO_2 with cerium oxide surface and the employment of CeO_2 as support and/or promoter in many catalytic reactions. However, not many authors investigated and quantified the adsorption capacity extensively, comparing materials with growing content of adsorbent phase and different supports (Al_2O_3 and ZSM-5) at three distinct temperatures. Previously, Yoshikawa *et al.* published some works on the CO_2 adsorption capacity of three different CeO_2 powders mixed with other CO_2 adsorbents materials, namely SiO_2, Al_2O_3 and ZrO_2 [96,97]. The results of their experiments highlighted the key role of the chemical adsorption sites for CO_2 together with other parameters such as morphology, particle size, porosity, and specific surface area, which could modify not only the number of adsorption sites available for the CO_2 chemical adsorption, but also the accessibility of these sites to CO_2 molecules [98]. Furthermore, Yoshikawa *et al.* observed that SiO_2 was characterized by a high surface area, but it exhibited the lowest amount of CO_2 adsorbed in comparison with the other selected oxides. On the other hand, the authors demonstrated that cerium oxide-based materials exhibit the largest amount of gas adsorbed.

In the present work, CO_2 adsorption experiments were performed at

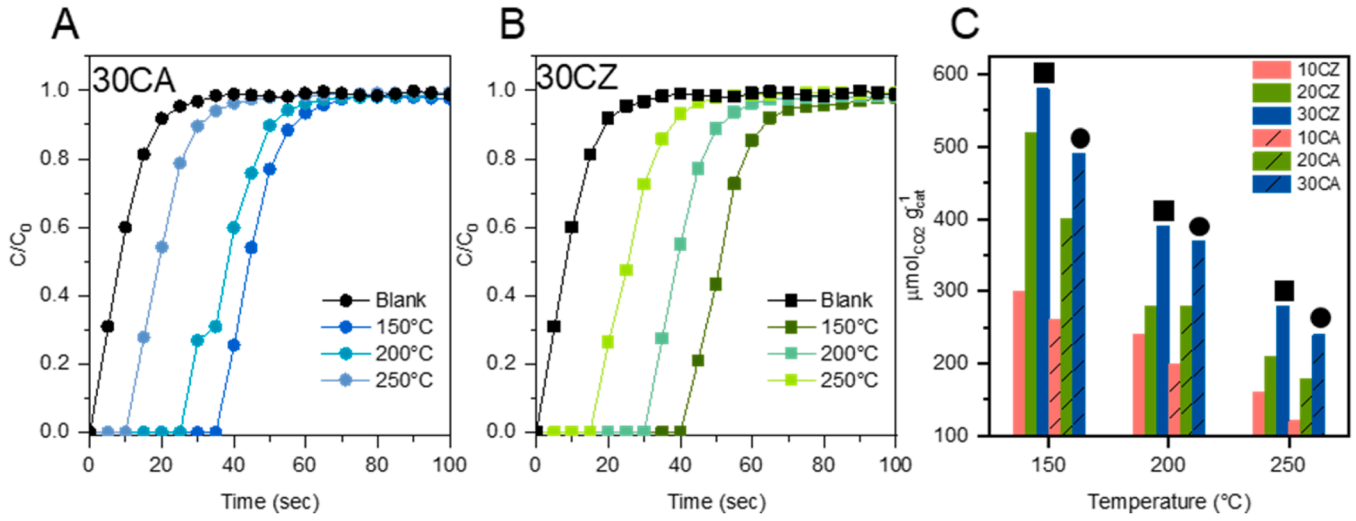

Fig. 7. Adsorption breakthrough curves of CO_2 for **A)** 30CA and **B)** 30CZ. **C)** CO_2 adsorption uptakes of the six samples derived from their corresponding experiment performed at 150, 200, and 250 °C.

three different temperatures (150, 200, and 250 °C) at atmospheric pressure, evaluating the disparities in gas uptake to study a possible new material employable in the adsorption and reduction of CO_2. Subsequently, the materials that showed the best results were selected for the functionalization with ruthenium to produce active catalysts for CO_2 methanation. To better understand the effects of temperature and cerium oxide loading, the breakthrough curves (BTCs) of 30CA and 30CZ are depicted in Fig. 7, along with a bar graph summarising the uptakes obtained from the adsorption experiments. The CO_2 adsorption uptake followed this trend for all three temperatures, considering the cerium oxide percentage loading: 10% < 20% < 30%. Another essential difference could be observed looking at the uptakes reached by the six materials. The decrease in adsorption capacity with increasing temperature revealed that the adsorption is an exothermic phenomenon, as expected for physical adsorption. Interestingly, the Al_2O_3-supported materials adsorbed lower quantities of CO_2 than the zeolite-supported ones (Table 5). The gap between adsorption capacities of xCA and xCZ does not seem associated with the actual content of ceria, since it is similar to the nominal one for both the sets of samples; instead, this property is likely linked to the dispersion role acted by the two supports, e.g., considering their different specific surface areas. For instance, the zeolite with 288 m^2/g (Table 2) favoured the formation not only of areas in which ceria was more abundant, but also of small CeO_2 spots of around 10 nm (not observed for Al_2O_3-supported materials), that could increase the surface sites able to adsorb and activate CO_2 (Fig. S6). Considering the role of the support, aluminium oxide is one of the most widely used supports for inorganic catalysts; nevertheless, to the best of our knowledge, only spectroscopic studies about interaction of CO_2 with Al_2O_3 were reported in the literature, without any effective quantitative data about CO_2 adsorption [99,100]. On the other hand, zeolite ZSM-5 featured a lower average pore size and a rich microporous structure, which allowed for the efficient physisorption of CO_2 via van der Waals forces and/or hydrogen bonding [101,102]. The longer breakthrough times for the 30CZ samples could be explained by considering the slower formation of more stable carbonate species along with a different mass transfer resistance between the two samples taking into account the individual pore sizes (Table 2). Having the highest adsorption capacity, 30CA and 30CZ were selected as composite materials for the subsequent impregnation step to synthetise ruthenium-loaded catalyst for the CO_2 conversion to methane.

Table 5
Adsorption capacities of the composite materials tested for CO_2 capture at ambient pressure and at different temperatures. The two pure supports (Al_2O_3 and ZSM-5) were tested in the same conditions as a comparison.

Samples	Adsorption Temperature (°C)	CO_2 Uptakes ($\mu mol_{CO_2} g_{cat}^{-1}$)	CO_2 Uptakes ($mmol_{CO_2} g_{CeO2}^{-1}$)
H-ZSM-5	150	120	
	200	80	—
	250	100	
10CZ	150	299	3.9
	200	240	3.2
	250	156	2.1
20CZ	150	525	2.8
	200	281	1.5
	250	209	1.1
30CZ	150	581	1.9
	200	390	1.3
	250	276	0.9
γ-Al_2O_3	150	159	
	200	110	—
	250	88	
10CA	150	263	3.2
	200	199	2.4
	250	120	1.5
20CA	150	396	2.0
	200	282	1.5
	250	179	0.9
30CA	150	486	1.6
	200	370	1.2
	250	245	0.8

For comparison purposes, the CO_2 uptake values of some materials used for CO_2 capture proposed in the literature were collected in Table S1. As stated before, examples of zeolite- and alumina-based materials used for applications at temperatures similar to those explored in this work can be scarcely found since, if not functionalised/doped, their adsorption capacity drops rapidly with increasing temperature. Considering ceria, there are not many studies examining the adsorptive capacity of this oxide at temperatures above 100 °C. In their work, Barroso Bogeat et al. prepared ceria-based nanomaterials coated with yttria (Y_2O_3) in order to modulate the surface acid-base and redox features and enhance CO_2 adsorption and activation properties. Using CO_2-TPD analysis, they observed that as-prepared materials were able to retain approximately 30 μmol g^{-1} of CO_2 after saturation at 25 °C (P_{CO2} = 1 atm) [103]. Therefore, the as-prepared composite materials in the present work greatly increased the CO_2 adsorption capacity of pure ceria and were also effective at temperatures that can be considered high for zeolites and aluminium oxides. Materials based on alkaline and alkaline earth metal oxides, i.e., layered double hydroxides/oxides (LDH/LDO) [104], demonstrate better performances at high temperatures due to their pronounced basicity. However, the operating temperature ranges typical of these materials are much higher (350–450 °C) with respect to the mild-temperature applications envisaged in this work.

3.2.2. Catalytic activity

CO_2 methanation experiments were performed with the ruthenium-impregned catalysts in the same fixed-bed reactor used for the carbon dioxide adsorption experiments. The gases time evolution profile is depicted in Fig. S7 in the supporting information file. As expected, all ruthenium-loaded catalysts were active for CO_2 methanation, with 100% selectivity to CH_4. Thermodynamically, CO_2 methanation is a spontaneous reaction for the formation of methane with water as a byproduct. The reaction is governed by a stoichiometric molar ratio of the reacting gases (H_2: CO_2 = 4: 1), according to Eq. (1) and can occur at a relatively low temperature (200–250 °C) and at atmospheric pressure.

As a whole, the conversion tests were carried out at 250 °C in order to simulate a realistic temperature of exhaust flue gases, keeping the same temperature used in the adsorption tests. Moreover, relative low process temperature were investigated to avoiding further disadvantaged the CO_2 adsorption process and preventing the production of the CO by-product (RWGS; $H_2 + CO_2 \rightarrow CO + H_2O$), that may occur at higher temperature [105]. Indeed, the conversion of CO_2 to methane is strongly exothermic ($\Delta H = -165.0$kJ/mol), therefore it is penalised at elevated reaction temperatures [105–107].

The methanation experiments were performed following the procedure explained in *Materials and methods*, by testing the catalysts in cyclic experiments. First of all, the catalysts were reduced by a stream of 5% H_2/N_2 at the beginning of test campaign, and this reduction step was then cyclically repeated after each CO_2 adsorption phase. The first hydrogenation allowed to reduce both the RuO_2 phase and a small part of the surface of cerium oxide, entailing the formation of metallic Ru and ceria superficial oxygen vacancies. It was observed that this first reductive treatment, which was not performed prior to the CO_2-TPD and adsorption experiments, is critical for methane yield. In experiments conducted without this first reduction (not reported in this paper), no methane production was observed. Wang et al. and López-Rodríguez et al. discovered that Ru generates new activation and conversion sites for CO_2 when it is in its reduced state [25,40]. The adsorption of CO_2 occurs on Ru in a dissociative form, forming weak poly-bonded carbonyl groups with Ru species. Conversely, CO_2 strongly adsorbed as carbonates on ceria surface oxygen sites (as observed in the spectra shown in Fig. 6) or as carboxylates (CO_2-δ) at the oxygen vacancies of reduced ceria, resulting in the reoxidation of ceria. These carbonates could evolve into CO which served as a reaction intermediate during the hydrogenation stage, cooperating to the overall CO_2 methanation process

[40]. After the adsorption step, the subsequent hydrogenative treatment was fundamental both for the catalytic conversion of the activated CO_2 molecules to methane and for the regeneration of ceria oxygen vacancies necessary for the following adsorption steps. Five consecutive cycles were conducted on 2R30CZ and 2R30CA and the results are reported through bar graphs in Fig. 8 and numerically in Table 6.

The zeolite-supported catalyst (section **A**) adsorbed ca. 100 μmol_{CO2} g^{-1} more CO_2 than the Al_2O_3-supported material, achieving a maximum value of 316 μmol_{CO2} g^{-1} in cycle C2. However, only a small fraction of the adsorbed gas was effectively converted to methane, whose value exceeded a hundred of μmol_{CH4} g^{-1} only in the last cycle (108 μmol_{CH4} g^{-1}). Conversely, 2R30CA (section **B**) captured approximately the same amount of CO_2 in each experiment, from a minimum of 194 μmol_{CO2} g^{-1} in cycle C2 to a maximum of 207 μmol_{CO2} g^{-1} in cycle C3. The CH_4 yield (in terms of produced CH_4 with respect to adsorbed CO_2) was characterized by an average value of 51% and reached the highest value in the first cycle (with 55% of adsorbed CO_2 converted). The amount of H_2 consumed during the catalytic methanation was in agreement with the stoichiometry of Sabatier's reaction, since it was in a 4:1 ratio with respect to CH_4 produced; this clearly confirmed that the redox nature of ceria did not have detrimental effects on the hydrogen consumption at mild temperature, in line with the H_2-TPR profiles in Fig. 4.

Methanation results could be interpreted by taking into consideration several outputs of the characterization techniques. ICP analysis revealed that a slightly higher amount of Ru species is present in the 2R30CA catalyst; nevertheless, if the quantity of CH_4 generated is normalized to the weight of Ru present in the two supported materials (Fig. S10) the specific activity of the catalyst supported on alumina remains equal or slightly lower than that of the zeolite-supported sample. Moreover, H_2-TPR analysis revealed that different types of RuOx species can be found in the two materials. The presence of a signal at lower temperature in the 2R30CA plot suggests the presence of well-dispersed particles of RuO_2 on ceria, strongly interacting with the adsorbent support. As reported by Safariamin et al., better Ru-Ce interactions and effective dispersions of the easily reducible metal on the support intensify the catalytic properties of the system [108]. Contrariwise, 2R30CZ has a lower Ru content and its H_2-TPR profile reveals a single reduction peak (with just a small shoulder), that may be attributable to Ru species with a high grade of crystallinity and weaker interactions with the ceria phase. XPS analysis revealed the presence of more Ru species (Ru^{n+}) interacting with Ce in 2R30CA (Table 2). TEM analysis also allowed to detect the presence of areas of 2R30CZ where only ceria is present while ruthenium is absent (Figs. S6). The partial separation between the adsorbent phase and the metal phase and the lower interaction between them may contribute to the lower catalytic activity of this catalyst as well. Therefore, the conversion yield was lower, reaching the top value in cycle 5 (32%). Even in this case, the stoichiometric ratio between consumed H_2 and produced CH_4 was kept. In the supporting information file, the results of cyclic methanation tests conducted on an unsupported 2Ru/CeO_2_rods catalyst are provided for comparison purpose (Fig. S9).

Table 6
Summary of the catalytic conversion of CO_2 to CH_4, in terms of CO_2 adsorbed, H_2 consumed during the catalytic reaction, CH_4 produced and the yield in percentage.

Catalysts	No. Test	CO_2 adsorbed ($\mu mol\ g^{-1}$)	H_2 consumed ($\mu mol\ g^{-1}$)	CH_4 produced ($\mu mol\ g^{-1}$)	Yield (%)
2R30CZ	C1	306	396	99	32
	C2	316	385	96	30
	C3	306	354	80	26
	C4	294	366	85	29
	C5	288	388	108	38
2R30CA	C1	202	451	111	55
	C2	194	444	99	51
	C3	207	422	94	45
	C4	203	408	105	52
	C5	196	429	100	51

4. Conclusions

This study focused on the investigation of different supported ceria-based materials, exploring their CO_2 adsorption capacities and their catalytic ability to convert CO_2 to methane after ruthenium functionalization. Six ceria-base materials were tested at three different temperatures (150, 200 and 250 °C) and the uptake results proved that an increment of the cerium oxide phase led to a greater amount of CO_2 adsorbed at the temperature ranges explored. The dynamic adsorption experiments highlighted the effects of two different supports on ceria dispersion and how the subsequent physico-chemical characteristics influenced the final results. In particular, the surface areas of the two supports affected the dispersion of the adsorbent phase, for example allowing the formation of nanometric ceria-spots on zeolite surface, which enhanced the performances of these materials. These findings demonstrate that these ceria-based composite materials can be effectively applied for carbon dioxide capture at temperatures that would be challenging for pristine CeO_2, zeolite or alumina. 30CA and 30CZ were subsequently impregned with ruthenium and the two DFMs were engaged in cyclic methanation tests. The results demonstrated that 2R30CA and 2R30CZ catalysts are highly selective towards methane and effective at ambient pressure, at temperatures lower than those reported in the literature for typical alkali- and alkali-earth based DFMs. 2R30CA exhibited the best performances in terms of CO_2 activation and

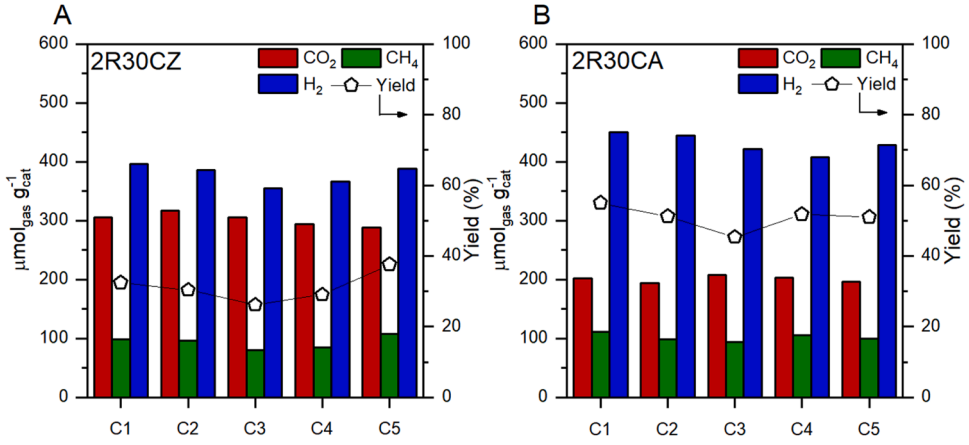

Fig. 8. Bar charts illustrating the methanation results obtained in five cyclic tests by **A)** 2R30CZ, **B)** 2R30CA, in terms of adsorbed CO_2, consumed H_2 during the catalytic reaction, produced CH_4, and the final yield in percentage.

conversion, thanks to a better metal-support interaction between ruthenium and cerium oxide, as confirmed by H_2-TPR and XPS. From these outcomes, it is possible to conclude that supported Ru-CeO_2 materials are promising suitable catalysts for the stepwise capture and conversion of CO_2 at mild temperatures and atmospheric pressure. The employment of such DFMs in the treatment of industrial flue gases relatively rich in CO_2 has great potential and could help in reducing greenhouse gases emissions and fighting climate change.

CRediT authorship contribution statement

Conceptualization: Marco Piumetti, Andrea Rizzetto; **Methodology**: Marco Piumetti, Andrea Rizzetto, Enrico Sartoretti; **Investigation**: Andrea Rizzetto, Enrico Sartoretti; **Funding acquisition**: Samir Bensaid, Raffaele Pirone, Marco Piumetti; **Resources**: Marco Piumetti, Samir Bensaid, Raffaele Pirone; **Writing and editing**: Andrea Rizzetto, Marco Piumetti, Enrico Sartoretti; **Supervision**: Marco Piumetti.

Declaration of Competing Interest

The authors declare that they have no known competing financial interests or personal relationships that could have appeared to influence the work reported in this paper.

Data Availability

Data will be made available on request.

Acknowledgements

The authors greatly thank Loris Bellero for helping in data collection during his MS thesis preparation. Camilla Galletti, Marco Allione and Salvatore Guastella are kindly acknowledged as well for performing XRD, FESEM, TEM and XPS analyses. The authors acknowledge the funding received by the Italian Ministero dell'Università e della Ricerca (MUR) under the Dipartimento di Eccellenza 2018–2022 program and the PON Ricerca e Innovazione "REACT-EU" project (DM 1062/21).

Appendix A. Supporting information

Supplementary data associated with this article can be found in the online version at doi:10.1016/j.cattod.2023.114478.

References

[1] E.S. Sanz-Pérez, C.R. Murdock, S.A. Didas, C.W. Jones, Direct capture of CO 2 from Ambient Air, Chem. Rev. 116 (2016) 11840–11876, https://doi.org/10.1021/acs.chemrev.6b00173.

[2] M. Bui, C.S. Adjiman, A. Bardow, E.J. Anthony, A. Boston, S. Brown, P.S. Fennell, S. Fuss, A. Galindo, L.A. Hackett, J.P. Hallett, H.J. Herzog, G. Jackson, J. Kemper, S. Krevor, G.C. Maitland, M. Matuszewski, I.S. Metcalfe, C. Petit, G. Puxty, J. Reimer, D.M. Reiner, E.S. Rubin, S.A. Scott, N. Shah, B. Smit, J.P.M. Trusler, P. Webley, J. Wilcox, N. Mac Dowell, Carbon capture and storage (CCS): the way forward, Energy Environ. Sci. 11 (2018) 1062–1176, https://doi.org/10.1039/C7EE02342A.

[3] I. Hussain, A.A. Jalil, N.S. Hassan, M.Y.S. Hamid, Recent advances in catalytic systems for CO_2 conversion to substitute natural gas (SNG): Perspective and challenges, J. Energy Chem. 62 (2021) 377–407, https://doi.org/10.1016/j.jechem.2021.03.040.

[4] M.T. Dunstan, F. Donat, A.H. Bork, C.P. Grey, C.R. Müller, CO 2 Capture at Medium to High Temperature Using Solid Oxide-Based Sorbents: Fundamental Aspects, Mechanistic Insights, and Recent Advances, Chem. Rev. 121 (2021) 12681–12745, https://doi.org/10.1021/acs.chemrev.1c00100.

[5] F. Hussin, M.K. Aroua, Recent trends in the development of adsorption technologies for carbon dioxide capture: A brief literature and patent reviews (2014–2018), J. Clean. Prod. 253 (2020), 119707, https://doi.org/10.1016/j.jclepro.2019.119707.

[6] I. Ghiat, T. Al-Ansari, A review of carbon capture and utilisation as a CO_2 abatement opportunity within the EWF nexus, J. CO_2 Util. 45 (2021), 101432, https://doi.org/10.1016/j.jcou.2020.101432.

[7] M. Zhu, Q. Ge, X. Zhu, Catalytic Reduction of CO_2 to CO via Reverse Water Gas Shift Reaction: Recent Advances in the Design of Active and Selective Supported Metal Catalysts, Trans. Tianjin Univ. 26 (2020) 172–187, https://doi.org/10.1007/s12209-020-00246-8.

[8] O. Elishav, Y. Shener, V. Beilin, M.V. Landau, M. Herskowitz, G.E. Shter, G. S. Grader, Electrospun Fe–Al–O nanobelts for selective CO 2 hydrogenation to light olefins, ACS Appl. Mater. Interfaces 12 (2020) 24855–24867, https://doi.org/10.1021/acsami.0c05765.

[9] J. Wei, Q. Ge, R. Yao, Z. Wen, C. Fang, L. Guo, H. Xu, J. Sun, Directly converting CO_2 into a gasoline fuel, Nat. Commun. 8 (2017), 15174, https://doi.org/10.1038/ncomms15174.

[10] C.G. Okoye-Chine, Conversion of carbon dioxide into fuels—a review 30 (2022).

[11] A. Weilhard, S.P. Argent, V. Sans, Efficient carbon dioxide hydrogenation to formic acid with buffering ionic liquids, Nat. Commun. 12 (2021), 231, https://doi.org/10.1038/s41467-020-20291-0.

[12] X.-X. Hou, C.-H. Xu, Y.-L. Liu, J.-J. Li, X.-D. Hu, J. Liu, J.-Y. Liu, Q. Xu, Improved methanol synthesis from CO_2 hydrogenation over CuZnAlZr catalysts with precursor pre-activation by formaldehyde, J. Catal. 379 (2019) 147–153, https://doi.org/10.1016/j.jcat.2019.09.025.

[13] F. Arena, K. Barbera, G. Italiano, G. Bonura, L. Spadaro, F. Frusteri, Synthesis, characterization and activity pattern of Cu–ZnO/ZrO2 catalysts in the hydrogenation of carbon dioxide to methanol, J. Catal. 249 (2007) 185–194, https://doi.org/10.1016/j.jcat.2007.04.003.

[14] G. Bonura, C. Cannilla, L. Frusteri, E. Catizzone, S. Todaro, M. Migliori, G. Giordano, F. Frusteri, Interaction effects between CuO-ZnO-ZrO2 methanol phase and zeolite surface affecting stability of hybrid systems during one-step CO_2 hydrogenation to DME, Catal. Today 345 (2020) 175–182, https://doi.org/10.1016/j.cattod.2019.08.014.

[15] F. Salomone, E. Sartoretti, S. Ballauri, M. Castellino, C. Novara, F. Giorgis, R. Pirone, S. Bensaid, CO_2 hydrogenation to methanol over Zr- and Ce-doped indium oxide, Catal. Today 423 (2023), 114023, https://doi.org/10.1016/j.cattod.2023.01.030.

[16] A.I. Latsiou, N.D. Charisiou, Z. Frontistis, A. Bansode, M.A. Goula, CO_2 hydrogenation for the production of higher alcohols: trends in catalyst developments, challenges and opportunities, Catal. Today 420 (2023), 114179, https://doi.org/10.1016/j.cattod.2023.114179.

[17] Q. Pan, J. Peng, T. Sun, S. Wang, S. Wang, Insight into the reaction route of CO_2 methanation: promotion effect of medium basic sites, Catal. Commun. 45 (2014) 74–78, https://doi.org/10.1016/j.catcom.2013.10.034.

[18] J. Yang Lim, J. McGregor, A.J. Sederman, J.S. Dennis, Kinetic studies of CO 2 methanation over a Ni/ γ -Al 2 O 3 catalyst using a batch reactor, Chem. Eng. Sci. 141 (2016) 28–45, https://doi.org/10.1016/j.ces.2015.10.026.

[19] L. Bian, L. Zhang, R. Xia, Z. Li, Enhanced low-temperature CO 2 methanation activity on plasma-prepared Ni-based catalyst, J. Nat. Gas. Sci. Eng. 27 (2015) 1189–1194, https://doi.org/10.1016/j.jngse.2015.09.066.

[20] M.A. Arellano-Treviño, Z. He, M.C. Libby, R.J. Farrauto, Catalysts and adsorbents for CO_2 capture and conversion with dual function materials: Limitations of Ni-containing DFMs for flue gas applications, J. CO_2 Util. 31 (2019) 143–151, https://doi.org/10.1016/j.jcou.2019.03.009.

[21] M.S. Duyar, CO_2 utilization with a novel dual function material (DFM) for capture and catalytic conversion to synthetic natural gas: An update 7 (2016).

[22] S. Ballauri, E. Sartoretti, M. Hu, C. D'Agostino, Z. Ge, L. Wu, C. Novara, F. Giorgis, M. Piumetti, D. Fino, N. Russo, S. Bensaid, Praseodymium doping in ceria-supported palladium nanocatalysts as an effective strategy to minimize the inhibiting effects of water during methane oxidation, Appl. Catal. B Environ. 320 (2023), 121898, https://doi.org/10.1016/j.apcatb.2022.121898.

[23] I.S. Omodolor, H.O. Otor, J.A. Andonegui, B.J. Allen, A.C. Alba-Rubio, Dual-function materials for CO_2 capture and conversion: a review, Ind. Eng. Chem. Res 20 (2020).

[24] A. Bermejo-López, B. Pereda-Ayo, J.A. González-Marcos, J.R. González-Velasco, Ni loading effects on dual function materials for capture and in-situ conversion of CO_2 to CH4 using CaO or Na2CO3, J. CO_2 Util. 34 (2019) 576–587, https://doi.org/10.1016/j.jcou.2019.08.011.

[25] S. Wang, E.T. Schrunk, H. Mahajan, R.J. Farrauto, The role of ruthenium in CO_2 capture and catalytic conversion to fuel by dual function materials (DFM), Catalysts 7 (2017) 88, https://doi.org/10.3390/catal7030088.

[26] F. Kosaka, Y. Liu, S.-Y. Chen, T. Mochizuki, H. Takagi, A. Urakawa, K. Kuramoto, Enhanced activity of integrated CO 2 capture and reduction to CH 4 under pressurized conditions toward atmospheric CO 2 utilization, ACS Sustain. Chem. Eng. 9 (2021) 3452–3463, https://doi.org/10.1021/acssuschemeng.0c07162.

[27] F. Wang, S. He, H. Chen, B. Wang, L. Zheng, M. Wei, D.G. Evans, X. Duan, Active site dependent reaction mechanism over Ru/CeO 2 catalyst toward CO 2 methanation, J. Am. Chem. Soc. 138 (2016) 6298–6305, https://doi.org/10.1021/jacs.6b02762.

[28] N.D. Charisiou, G. Siakavelas, L. Tzounis, V. Sebastian, A. Monzon, M.A. Baker, S. J. Hinder, K. Polychronopoulou, I.V. Yentekakis, M.A. Goula, An in depth investigation of deactivation through carbon formation during the biogas dry reforming reaction for Ni supported on modified with CeO2 and La2O3 zirconia catalysts, Int. J. Hydrog. Energy 43 (2018) 18955–18976, https://doi.org/10.1016/j.ijhydene.2018.08.074.

[29] M. Boaro, S. Colussi, A. Trovarelli, Ceria-based materials in hydrogenation and reforming reactions for CO_2 valorization, Front. Chem. 7 (2019), 28, https://doi.org/10.3389/fchem.2019.00028.

[30] S. Tada, T. Shimizu, H. Kameyama, T. Haneda, R. Kikuchi, Ni/CeO2 catalysts with high CO_2 methanation activity and high CH4 selectivity at low temperatures, Int. J. Hydrog. Energy 37 (2012) 5527–5531, https://doi.org/10.1016/j.ijhydene.2011.12.122.

[31] T. Das, G. Deo, Effects of metal loading and support for supported cobalt catalyst, Catal. Today 198 (2012) 116–124, https://doi.org/10.1016/j.cattod.2012.04.028.

[32] L. Atzori, M.G. Cutrufello, D. Meloni, R. Monaci, C. Cannas, D. Gazzoli, M.F. Sini, P. Deiana, E. Rombi, CO 2 methanation on hard-templated NiO CeO 2 mixed oxides, Int. J. Hydrog. Energy 42 (2017) 20689–20702, https://doi.org/10.1016/j.ijhydene.2017.06.198.

[33] J. Díez-Ramírez, P. Sánchez, V. Kyriakou, S. Zafeiratos, G.E. Marnellos, M. Konsolakis, F. Dorado, Effect of support nature on the cobalt-catalyzed CO_2 hydrogenation, J. CO_2 Util. 21 (2017) 562–571, https://doi.org/10.1016/j.jcou.2017.08.019.

[34] J.A.H. Dreyer, P. Li, L. Zhang, G.K. Beh, R. Zhang, P.H.-L. Sit, W.Y. Teoh, Influence of the oxide support reducibility on the CO_2 methanation over Ru-based catalysts, Appl. Catal. B Environ. 219 (2017) 715–726, https://doi.org/10.1016/j.apcatb.2017.08.011.

[35] C. Fukuhara, K. Hayakawa, Y. Suzuki, W. Kawasaki, R. Watanabe, A novel nickel-based structured catalyst for CO 2 methanation: a honeycomb-type Ni/CeO 2 catalyst to transform greenhouse gas into useful resources, Appl. Catal. Gen. 532 (2017) 12–18, https://doi.org/10.1016/j.apcata.2016.11.036.

[36] N.M. Martin, P. Velin, M. Skoglundh, M. Bauer, P.-A. Carlsson, Catalytic hydrogenation of CO $_2$ to methane over supported Pd, Rh and Ni catalysts, Catal. Sci. Technol. 7 (2017) 1086–1094, https://doi.org/10.1039/C6CY02536F.

[37] M. Li, H. Amari, A.C. van Veen, Metal-oxide interaction enhanced CO_2 activation in methanation over ceria supported nickel nanocrystallites, Appl. Catal. B Environ. 239 (2018) 27–35, https://doi.org/10.1016/j.apcatb.2018.07.074.

[38] Z. Bian, Y.M. Chan, Y. Yu, S. Kawi, Morphology dependence of catalytic properties of Ni/CeO2 for CO_2 methanation: a kinetic and mechanism study, Catal. Today 347 (2020) 31–38, https://doi.org/10.1016/j.cattod.2018.04.067.

[39] S. López-Rodríguez, A. Davó-Quiñonero, E. Bailón-García, D. Lozano-Castelló, A. Bueno-López, Effect of Ru loading on Ru/CeO2 catalysts for CO_2 methanation, Mol. Catal. 515 (2021), 111911, https://doi.org/10.1016/j.mcat.2021.111911.

[40] S. López-Rodríguez, A. Davó-Quiñonero, E. Bailón-García, D. Lozano-Castelló, F. C. Herrera, E. Pellegrin, C. Escudero, M. García-Melchor, A. Bueno-López, Elucidating the role of the metal catalyst and oxide support in the Ru/CeO $_2$ -catalyzed CO $_2$ methanation mechanism, J. Phys. Chem. C. 125 (2021) 25533–25544, https://doi.org/10.1021/acs.jpcc.1c07537.

[41] A.H. Zamani, R. Ali, W.A.W. Abu Bakar, Optimization of CO_2 methanation reaction over M*/Mn/Cu–Al2O3 (M*: Pd, Rh and Ru) catalysts, J. Ind. Eng. Chem. 29 (2015) 238–248, https://doi.org/10.1016/j.jiec.2015.02.028.

[42] P. Panagiotopoulou, Hydrogenation of CO 2 over supported noble metal catalysts, Appl. Catal. Gen. 542 (2017) 63–70, https://doi.org/10.1016/j.apcata.2017.05.026.

[43] A. Sápi, T. Rajkumar, M. Ábel, A. Efremova, A. Grósz, A. Gyuris, K.B. Ábrahámné, I. Szenti, J. Kiss, T. Varga, Á. Kukovecz, Z. Kónya, Noble-metal-free and Pt nanoparticles-loaded, mesoporous oxides as efficient catalysts for CO_2 hydrogenation and dry reforming with methane, J. CO_2 Util. 32 (2019) 106–118, https://doi.org/10.1016/j.jcou.2019.04.004.

[44] K. Tomishige, M. Asadullah, K. Kunimori, Syngas production by biomass gasification using Rh/CeO2/SiO2 catalysts and fluidized bed reactor, Catal. Today 89 (2004) 389–403, https://doi.org/10.1016/j.cattod.2004.01.002.

[45] K.O. Xavier, R. Sreekala, K.K.A. Rashid, K.K.M. Yusuff, B. Sen, Doping effects of cerium oxide on Ni/Al2O3 catalysts for methanation, Catal. Today 49 (1999) 17–21, https://doi.org/10.1016/S0920-5861(98)00403-9.

[46] S. Tada, O.J. Ochieng, R. Kikuchi, T. Haneda, H. Kameyama, Promotion of CO_2 methanation activity and CH4 selectivity at low temperatures over Ru/CeO2/Al2O3 catalysts, Int. J. Hydrog. Energy 39 (2014) 10090–10100, https://doi.org/10.1016/j.ijhydene.2014.04.133.

[47] H. Pérez-Pastenes, C.A. Barrales-Cortés, T. Viveros, Al2O3-CeO2 oxides: synthesis, characterization and evaluation as catalytic supports in benzene combustion. surface ceria effects, Int. J. Chem. React. Eng. 15 (2017), https://doi.org/10.1515/ijcre-2017-0143.

[48] C. Wu, P.T. Williams, Ni/CeO2/ZSM-5 catalysts for the production of hydrogen from the pyrolysis–gasification of polypropylene, Int. J. Hydrog. Energy 34 (2009) 6242–6252, https://doi.org/10.1016/j.ijhydene.2009.05.121.

[49] B. Dou, G. Lv, C. Wang, Q. Hao, K. Hui, Cerium doped copper/ZSM-5 catalysts used for the selective catalytic reduction of nitrogen oxide with ammonia, Chem. Eng. J. 270 (2015) 549–556, https://doi.org/10.1016/j.cej.2015.02.004.

[50] C. Binet, M. Daturi, J.-C. Lavalley, IR study of polycrystalline ceria properties in oxidised and reduced states, Catal. Today 19 (1999).

[51] G.N. Vayssilov, M. Mihaylov, P.St Petkov, K.I. Hadjiivanov, K.M. Neyman, Reassignment of the vibrational spectra of carbonates, formates, and related surface species on ceria: a combined density functional and infrared spectroscopy investigation, J. Phys. Chem. C. 115 (2011) 23435–23454, https://doi.org/10.1021/jp208050a.

[52] D.C. Upham, A.R. Derk, S. Sharma, H. Metiu, E.W. McFarland, CO $_2$ methanation by Ru-doped ceria: the role of the oxidation state of the surface, Catal. Sci. Technol. 5 (2015) 1783–1791, https://doi.org/10.1039/C4CY01106F.

[53] T. Andana, M. Piumetti, S. Bensaid, L. Veyre, C. Thieuleux, N. Russo, D. Fino, E. A. Quadrelli, R. Pirone, Nanostructured equimolar ceria-praseodymia for NOx-assisted soot oxidation: insight into Pr dominance over Pt nanoparticles and metal–support interaction, Appl. Catal. B Environ. 226 (2018) 147–161, https://doi.org/10.1016/j.apcatb.2017.12.048.

[54] M. Thommes, K. Kaneko, A.V. Neimark, J.P. Olivier, F. Rodriguez-Reinoso, J. Rouquerol, K.S.W. Sing, Physisorption of gases, with special reference to the evaluation of surface area and pore size distribution (IUPAC Technical Report), Pure Appl. Chem. 87 (2015) 1051–1069, https://doi.org/10.1515/pac-2014-1117.

[55] E. Sartoretti, C. Novara, A. Chiodoni, F. Giorgis, M. Piumetti, S. Bensaid, N. Russo, D. Fino, Nanostructured ceria-based catalysts doped with La and Nd: How acid-base sites and redox properties determine the oxidation mechanisms, Catal. Today 390–391 (2022) 117–134, https://doi.org/10.1016/j.cattod.2021.11.040.

[56] C.M. Sims, R.A. Maier, A.C. Johnston-Peck, J.M. Gorham, V.A. Hackley, B. C. Nelson, Approaches for the quantitative analysis of oxidation state in cerium oxide nanomaterials, Nanotechnology 30 (2019), 085703, https://doi.org/10.1088/1361-6528/aae364.

[57] M. Cai, X. Bian, F. Xie, W. Wu, P. Cen, Preparation and performance of cerium-based catalysts for selective catalytic reduction of nitrogen oxides: a critical review, Catalysts 11 (2021) 361, https://doi.org/10.3390/catal11030361.

[58] G.B. Della Mea, L.P. Matte, A.S. Thill, F.O. Lobato, E.V. Benvenutti, L.T. Arenas, A. Jürgensen, R. Hergenröder, F. Poletto, F. Bernardi, Tuning the oxygen vacancy population of cerium oxide (CeO2−x, 0 <x<0.5) nanoparticles, Appl. Surf. Sci. 422 (2017) 1102–1112, https://doi.org/10.1016/j.apsusc.2017.06.101.

[59] E. Bêche, P. Charvin, D. Perarnau, S. Abanades, G. Flamant, Ce 3d XPS investigation of cerium oxides and mixed cerium oxide (CexTiyOz), Surf. Interface Anal. 40 (2008) 264–267, https://doi.org/10.1002/sia.2686.

[60] X. Qin, X. Chen, M. Chen, J. Zhang, H. He, C. Zhang, Highly efficient Ru/CeO $_2$ catalysts for formaldehyde oxidation at low temperature and the mechanistic study, Catal. Sci. Technol. 11 (2021) 1914–1921, https://doi.org/10.1039/D0CY01894E.

[61] D.J. Morgan, Resolving ruthenium: XPS studies of common ruthenium materials, Surf. Interface Anal. 47 (2015) 1072–1079, https://doi.org/10.1002/sia.5852.

[62] E. Demir, S. Akbayrak, A.M. Önal, S. Özkar, Nanoceria-supported ruthenium(0) nanoparticles: highly active and stable catalysts for hydrogen evolution from water, ACS Appl. Mater. Interfaces 10 (2018) 6299–6308, https://doi.org/10.1021/acsami.7b17469.

[63] Y. Guo, S. Mei, K. Yuan, D.-J. Wang, H.-C. Liu, C.-H. Yan, Y.-W. Zhang, Low-temperature CO $_2$ methanation over CeO $_2$ -supported ru single atoms, nanoclusters, and nanoparticles competitively tuned by strong metal–support interactions and H-spillover effect, ACS Catal. 8 (2018) 6203–6215, https://doi.org/10.1021/acscatal.7b04469.

[64] J. Li, Z. Liu, D.A. Cullen, W. Hu, J. Huang, L. Yao, Z. Peng, P. Liao, R. Wang, Distribution and valence state of Ru species on CeO $_2$ supports: support shape effect and its influence on CO oxidation, ACS Catal. 9 (2019) 11088–11103, https://doi.org/10.1021/acscatal.9b03113.

[65] F. Liang, Y. Yu, W. Zhou, X. Xu, Z. Zhu, Highly defective CeO $_2$ as a promoter for efficient and stable water oxidation, J. Mater. Chem. A. 3 (2015) 634–640, https://doi.org/10.1039/C4TA05770H.

[66] D. Mukherjee, B.G. Rao, B.M. Reddy, CO and soot oxidation activity of doped ceria: Influence of dopants, Appl. Catal. B Environ. 197 (2016) 105–115, https://doi.org/10.1016/j.apcatb.2016.03.042.

[67] X. Li, B. Yan, J. Zhang, N. Xu, J. Tao, R. Zhang, B. Liu, Z. Sun, G. Chen, Hydrogen production by aqueous phase reforming of phenol derived from lignin pyrolysis over NiCe/ZSM-5 catalysts, Int. J. Hydrog. Energy 43 (2018) 649–658, https://doi.org/10.1016/j.ijhydene.2017.09.096.

[68] N.D. Charisiou, Studying the stability of Ni supported on modified with CeO2 alumina catalysts for the biogas dry reforming reaction, Mater. Today 10 (2018).

[69] S. Wang, L. Zhao, W. Wang, Y. Zhao, G. Zhang, X. Ma, J. Gong, Morphology control of ceria nanocrystals for catalytic conversion of CO_2 with methanol 7 (2013).

[70] B. Azambre, L. Zenboury, J.V. Weber, P. Burg, Surface characterization of acidic ceria–zirconia prepared by direct sulfation, Appl. Surf. Sci. 12 (2010).

[71] T. Andana, M. Piumetti, S. Bensaid, N. Russo, D. Fino, R. Pirone, CO and Soot Oxidation over Ce-Zr-Pr Oxide Catalysts, Nanoscale Res. Lett. 11 (2016), 278, https://doi.org/10.1186/s11671-016-1494-6.

[72] T. Caputo, L. Lisi, R. Pirone, G. Russo, On the role of redox properties of CuO/CeO2 catalysts in the preferential oxidation of CO in H2-rich gases, Appl. Catal. Gen. 348 (2008) 42–53, https://doi.org/10.1016/j.apcata.2008.06.025.

[73] P. Miceli, S. Bensaid, N. Russo, D. Fino, CeO2-based catalysts with engineered morphologies for soot oxidation to enhance soot-catalyst contact, Nanoscale Res. Lett. 9 (2014), 254, https://doi.org/10.1186/1556-276X-9-254.

[74] M. Piumetti, S. Bensaid, N. Russo, D. Fino, Nanostructured ceria-based catalysts for soot combustion: investigations on the surface sensitivity, Appl. Catal. B Environ. 165 (2015) 742–751, https://doi.org/10.1016/j.apcatb.2014.10.062.

[75] A. Trovarelli, Catalytic properties of ceria and CeO $_2$ -containing materials, Catal. Rev. 38 (1996) 439–520, https://doi.org/10.1080/01614949608006464.

[76] K. Kubo, H. Iida, S. Namba, A. Igarashi, Comparison of steaming stability of Cu-ZSM-5 with those of Ag-ZSM-5, P/H-ZSM-5, and H-ZSM-5 zeolites as naphtha cracking catalysts to produce light olefin at high temperatures, Appl. Catal. Gen. 489 (2015) 272–279, https://doi.org/10.1016/j.apcata.2014.10.041.

[77] Q. Dai, W. Wang, X. Wang, G. Lu, Sandwich-structured CeO2@ZSM-5 hybrid composites for catalytic oxidation of 1, 2-dichloroethane: an integrated solution to coking and chlorine poisoning deactivation, Appl. Catal. B Environ. 203 (2017) 31–42, https://doi.org/10.1016/j.apcatb.2016.10.009.

[78] M. Jiang, B. Wang, Y. Yao, Z. Li, X. Ma, S. Qin, Q. Sun, A comparative study of CeO2-Al2O3 support prepared with different methods and its application on MoO3/CeO2-Al2O3 catalyst for sulfur-resistant methanation, Appl. Surf. Sci. 285 (2013) 267–277, https://doi.org/10.1016/j.apsusc.2013.08.049.

[79] J. Li, Z. Liu, R. Wang, Support structure and reduction treatment effects on CO oxidation of SiO2 nanospheres and CeO2 nanorods supported ruthenium catalysts, J. Colloid Interface Sci. 531 (2018) 204–215, https://doi.org/10.1016/j.jcis.2018.07.046.

[80] M. Piumetti, S. Bensaid, T. Andana, N. Russo, R. Pirone, D. Fino, Cerium-copper oxides prepared by solution combustion synthesis for total oxidation reactions: From powder catalysts to structured reactors, Appl. Catal. B Environ. 205 (2017) 455–468, https://doi.org/10.1016/j.apcatb.2016.12.054.
[81] M. Piumetti, Molecular Dynamics and Complexity in Catalysis and Biocatalysis, Springer International Publishing, Cham, 2022, https://doi.org/10.1007/978-3-030-88500-7.
[82] S. Navarro-Jaén, J.C. Navarro, L.F. Bobadilla, M.A. Centeno, O.H. Laguna, J. A. Odriozola, Size-tailored Ru nanoparticles deposited over γ-Al2O3 for the CO_2 methanation reaction, Appl. Surf. Sci. 483 (2019) 750–761, https://doi.org/10.1016/j.apsusc.2019.03.248.
[83] W. Wu, E. Weitz, Modification of acid sites in ZSM-5 by ion-exchange: an in-situ FTIR study, Appl. Surf. Sci. 316 (2014) 405–415, https://doi.org/10.1016/j.apsusc.2014.07.194.
[84] L. Lin, X. Zhang, N. He, J. Liu, Q. Xin, H. Guo, Operando dual beam FTIR study of hydroxyl groups and zn species over defective HZSM-5 zeolite supported zinc catalysts, Catalysts 9 (2019) 100, https://doi.org/10.3390/catal9010100.
[85] M. Piumetti, S. Bensaid, D. Fino, N. Russo, Nanostructured ceria-zirconia catalysts for CO oxidation: study on surface properties and reactivity, Appl. Catal. B Environ. 197 (2016) 35–46, https://doi.org/10.1016/j.apcatb.2016.02.023.
[86] T.R. Sahoo, M. Armandi, R. Arletti, M. Piumetti, S. Bensaid, M. Manzoli, S. R. Panda, B. Bonelli, Pure and Fe-doped CeO2 nanoparticles obtained by microwave assisted combustion synthesis: physico-chemical properties ruling their catalytic activity towards CO oxidation and soot combustion, Appl. Catal. B Environ. 211 (2017) 31–45, https://doi.org/10.1016/j.apcatb.2017.04.032.
[87] M.Y. Mihaylov, E.Z. Ivanova, G.N. Vayssilov, K.I. Hadjiivanov, Revisiting ceria-NOx interaction: FTIR studies, Catal. Today 357 (2020) 613–620, https://doi.org/10.1016/j.cattod.2019.05.014.
[88] A. Badri, C. Binet, J.-C. Lavalley, An FTIR study of surface ceria hydroxy groups during a redox process with H2, J. Chem. Soc. Faraday Trans. 92 (1996) 4669, https://doi.org/10.1039/ft9969204669.
[89] E. Davarpanah, M. Armandi, S. Hernández, D. Fino, R. Arletti, S. Bensaid, M. Piumetti, CO_2 capture on natural zeolite clinoptilolite: Effect of temperature and role of the adsorption sites, J. Environ. Manag. 275 (2020), 111229, https://doi.org/10.1016/j.jenvman.2020.111229.
[90] E.-M. Köck, M. Kogler, T. Bielz, B. Klötzer, S. Penner, In Situ FT-IR spectroscopic study of CO $_2$ and CO adsorption on Y $_2$ O $_3$, ZrO $_2$, and Yttria-stabilized ZrO $_2$, J. Phys. Chem. C. 117 (2013) 17666–17673, https://doi.org/10.1021/jp405625x.
[91] A. Cárdenas-Arenas, A. Quindimil, A. Davó-Quiñonero, E. Bailón-García, D. Lozano-Castelló, U. De-La-Torre, B. Pereda-Ayo, J.A. González-Marcos, J. R. González-Velasco, A. Bueno-López, Isotopic and in situ DRIFTS study of the CO_2 methanation mechanism using Ni/CeO2 and Ni/Al2O3 catalysts, Appl. Catal. B Environ. 265 (2020), 118538, https://doi.org/10.1016/j.apcatb.2019.118538.
[92] F. Wang, C. Li, X. Zhang, M. Wei, D.G. Evans, X. Duan, Catalytic behavior of supported Ru nanoparticles on the {1 0 0}, {1 1 0}, and {1 1 1} facet of CeO2, J. Catal. 329 (2015) 177–186, https://doi.org/10.1016/j.jcat.2015.05.014.
[93] L. Proaño, E. Tello, M.A. Arellano-Trevino, S. Wang, R.J. Farrauto, M. Cobo, In-situ DRIFTS study of two-step CO_2 capture and catalytic methanation over Ru,"Na2O"/Al2O3 dual functional material, Appl. Surf. Sci. 479 (2019) 25–30, https://doi.org/10.1016/j.apsusc.2019.01.281.
[94] S. Sun, H. Sun, S. Guan, S. Xu, C. Wu, Integrated CO_2 capture and methanation on Ru/CeO2-MgO combined materials: Morphology effect from CeO2 support, Fuel 317 (2022), 123420, https://doi.org/10.1016/j.fuel.2022.123420.
[95] P. Panagiotopoulou, D.I. Kondarides, X.E. Verykios, Mechanistic study of the selective methanation of CO over Ru/TiO $_2$ catalyst: identification of active surface species and reaction pathways, J. Phys. Chem. C. 115 (2011) 1220–1230, https://doi.org/10.1021/jp106538z.
[96] K. Yoshikawa, H. Sato, M. Kaneeda, J.N. Kondo, Synthesis and analysis of CO_2 adsorbents based on cerium oxide, J. CO_2 Util. 8 (2014) 34–38, https://doi.org/10.1016/j.jcou.2014.10.001.
[97] K. Yoshikawa, M. Kaneeda, H. Nakamura, Development of Novel CeO2-based CO_2 adsorbent and analysis on its CO_2 adsorption and desorption mechanism, Energy Procedia 114 (2017) 2481–2487, https://doi.org/10.1016/j.egypro.2017.03.1400.
[98] C. Slostowski, S. Marre, P. Dagault, O. Babot, T. Toupance, C. Aymonier, CeO 2 nanopowders as solid sorbents for efficient CO 2 capture/release processes, J. CO_2 Util. 20 (2017) 52–58, https://doi.org/10.1016/j.jcou.2017.03.023.
[99] C. Weilach, C. Spiel, K. Föttinger, G. Rupprechter, Carbonate formation on Al2O3 thin film model catalyst supports, Surf. Sci. 605 (2011) 1503–1509, https://doi.org/10.1016/j.susc.2011.05.025.
[100] J. Szanyi, J.H. Kwak, Dissecting the steps of CO $_2$ reduction: 1. The interaction of CO and CO $_2$ with γ-Al $_2$ O $_3$: an in situ FTIR study, Phys. Chem. Chem. Phys. 16 (2014) 15117–15125, https://doi.org/10.1039/C4CP00616J.
[101] S. Kumar, R. Srivastava, J. Koh, Utilization of zeolites as CO_2 capturing agents: advances and future perspectives, J. CO_2 Util. 41 (2020), 101251, https://doi.org/10.1016/j.jcou.2020.101251.
[102] S.M.W. Wilson, F.H. Tezel, CO $_2$ and CO adsorption equilibrium on ZSM-5 for different SiO $_2$ /Al $_2$ O $_3$ ratios, Sep. Sci. Technol. 54 (2019) 722–730, https://doi.org/10.1080/01496395.2018.1518332.
[103] A. Barroso Bogeat, G. Blanco, J.M. Pintado, D. Goma, J.J. Calvino Gámez, Tailoring CO_2 adsorption and activation properties of ceria nanocubes by coating with nanometre-thick yttria layers, Surf. Interfaces 26 (2021), 101353, https://doi.org/10.1016/j.surfin.2021.101353.
[104] Q. Wang, Z. Wu, H.H. Tay, L. Chen, Y. Liu, J. Chang, Z. Zhong, J. Luo, A. Borgna, High temperature adsorption of CO_2 on Mg–Al hydrotalcite: Effect of the charge compensating anions and the synthesis pH, Catal. Today 164 (2011) 198–203, https://doi.org/10.1016/j.cattod.2010.10.042.
[105] J. Gao, Y. Wang, Y. Ping, D. Hu, G. Xu, F. Gu, F. Su, A thermodynamic analysis of methanation reactions of carbon oxides for the production of synthetic natural gas, RSC Adv. 2 (2012) 2358, https://doi.org/10.1039/c2ra00632d.
[106] K. Stangeland, D. Kalai, H. Li, Z. Yu, CO 2 methanation: the effect of catalysts and reaction conditions, Energy Procedia 105 (2017) 2022–2027, https://doi.org/10.1016/j.egypro.2017.03.577.
[107] F. Meng, X. Li, X. Lv, Z. Li, CO hydrogenation combined with water-gas-shift reaction for synthetic natural gas production: a thermodynamic and experimental study, Int. J. Coal Sci. Technol. 5 (2018) 439–451, https://doi.org/10.1007/s40789-017-0177-y.
[108] M. Safariamin, L.H. Tidahy, E. Abi-Aad, S. Siffert, A. Aboukaïs, Dry reforming of methane in the presence of ruthenium-based catalysts, Comptes Rendus Chim. 12 (2009) 748–753, https://doi.org/10.1016/j.crci.2008.10.021.